Coseismic uplift as strandplain-building mechanism: morphodynamic and stratigraphic evidence from the 2010 Maule earthquake, south-central Chile

Authors

Cristian Araya-Cornejo[1,2*]

[1]Instituto de Geografía, Pontificia Universidad Católica de Chile, Santiago, Chile

[2]Centro UC Observatorio de la Costa, PUC, Santiago, Chile

*Corresponding author: ciaraya2@uc.cl

Diego Aedo[3,4,5]

[3]Escuela de Geología, Universidad Andrés Bello, Concepción, Chile

[4]Millennium Institute of Oceanography, Concepción, Chile

[5]Instituto de Ciencias de la Tierra, Universidad Austral de Chile, Valdivia, Chile

Carolina Martínez[1,2,6]

[6]Instituto Milenio en Socio-Ecología Costera (SECOS), Santiago, Chile

Daniel Melnick[4,5]

César Araya[4,7]

[7]Instituto de Geografía, Pontificia Universidad Católica de Valparaíso, Valparaíso, Chile

Matías Carvajal[4,7]

Arturo Belmonte[8]

[8]Departamento de Geofísica, Universidad de Concepción, Concepción, Chile

Marcos Moreno[9]

[9]Departamento de Ingeniería Estructural y Geotécnica, Pontificia Universidad Católica de Chile, Santiago, Chile

Jorge Qüense[1,2]

Coseismic uplift as strandplain-building mechanism: morphodynamic and stratigraphic evidence from the 2010 Maule earthquake, south-central Chile

Cristian Araya-Cornejo (1,2)*, Diego Aedo (3,4,5), Carolina Martínez (1,2,6), Daniel Melnick (4,5), César Araya (4,7), Matías Carvajal (4,7), Arturo Belmonte (8), Marcos Moreno (9), Jorge Qüense (1,2)

(1) Instituto de Geografía, Pontificia Universidad Católica de Chile, Santiago, Chile ciaraya2@uc.cl

(2) Centro UC Observatorio de la Costa, Pontificia Universidad Católica de Chile, Santiago, Chile

(3) Escuela de Geología, Universidad Andrés Bello, Concepción, Chile

(4) Millennium Institute of Oceanography, Concepción, Chile

(5) Instituto de Ciencias de La Tierra, Universidad Austral de Chile, Valdivia, Chile

(6) Instituto Milenio en Socio-Ecología Costera (SECOS), Santiago, Chile

(7) Instituto de Geografía, Pontificia Universidad Católica de Valparaíso, Valparaíso, Chile

(8) Departamento de Geofísica, Universidad de Concepción, Concepción, Chile

(9) Departamento de Ingeniería Estructural y Geotécnica, Pontificia Universidad Católica de Chile, Santiago, Chile

Highlights

- First multi-proxy human-timescale evidence of coseismic strandplain construction.
- Post-seismic SVDL advance (45–48 m) is consistent with inter-ridge spacing (48.9 m).
- GPR reveals a replicable beach–berm succession consistent with seismic cyclicity.
- Coseismic uplift buffers sediment starvation and interseismic subsidence.
- Interseismic subsidence (−9.8 to −16.5 mm yr^{-1}) underscores the tectonic buffer role.

Abstract

Coseismic uplift along convergent margins drives rapid coastal progradation, yet its short-term morpho-stratigraphic response remains poorly documented at human timescales. Here we integrate four complementary high-resolution proxies: satellite-derived shorelines, multi-temporal mapping of the seaward dune vegetation line (SVDL), ground-penetrating radar stratigraphy, and UAV–LiDAR topographic surveys to reconstruct 15 years of post-seismic coastal evolution at Laraquete–Horcones Beach following the 2010 Mw 8.8 Maule earthquake. Pre-seismic records confirm a sediment-starved coast lacking long-term progradation. The earthquake produced an instantaneous shoreline advance of 25 ± 4.9 m, followed by sustained post-seismic SVDL progradation of 45–48 m. This distance closely matches the mean inter-ridge spacing of the adjacent Holocene Laraquete–Carampangue strandplain (48.9 m). GPR data reveal a replicable prograding beach–berm stratigraphic succession (PBF→BBF), locally capped by an aeolian drape, with abrupt landward signal attenuation indicating rapid coastal abandonment and subaerial stabilization. By integrating short-term morphodynamics with subsurface stratigraphy, these results provide the first multi-proxy observational evidence consistent with repeated coseismic uplift driving Holocene strandplain construction along sediment-limited convergent margins, supporting this mechanism as a first-order control in sediment-starved convergent settings. Coseismic uplift thus functions as a recurring tectonic buffer, temporarily offsetting sediment deficits and interseismic subsidence, with implications for coastal resilience under sea-level rise.

Keywords: Coseismic uplift, post-seismic progradation, strandplain, beach-ridge formation.

1. Introduction

Coasts located on tectonically active margins can experience dramatic changes following large-magnitude earthquakes due to abrupt uplift or subsidence (Pirazzoli, 1995; Plafker and Savage, 1969). Coseismic uplift generates an instantaneous relative sea-level fall, forcing the coastal system to seek a new equilibrium (Aedo et al., 2023; Anthony and Aagaard, 2020; Cowell and Thom, 1995; Martínez et al., 2015; Tamura et al., 2007). Such responses have been documented after the 1964 Alaska earthquake (Kirkby and Kirkby, 1969; Stanley, 1968), the 2016 Kaikōura event in New Zealand (MacDonald et al., 2023), and the 2011 Tohoku-oki and 2024 Noto Peninsula earthquakes in Japan (Richmond et al., 2012; Tanaka et al., 2012; Tsunetaka et al., 2024), highlighting the widespread impact of tectonic perturbations on coastal evolution.

Following coseismic uplift, marine and aeolian dynamics couple intensively, driving coastal reconstruction (Aedo et al., 2023; Cohn et al., 2018). The sudden widening of the dry beach and intertidal zone increases the aeolian fetch, facilitating the transport of large volumes of newly exposed sediment toward the backshore (Bauer and Davidson-Arnott, 2003). This beach–aeolian coupling promotes the accelerated development of aeolian landforms, such as sand sheets and nebkhas, driven by the trapping of wind-blown sediments by pioneer vegetation and the pre-existing topography (Aedo et al., 2023; Hesp, 2002).

The long-term geomorphological evolution of the south-central Chilean coast is strongly governed by the historical recurrence of subduction megathrust earthquakes (e.g., in 1570, 1657, 1751, 1835, and 2010), which generate meter-scale coseismic uplift (San Martín et al., 2024; Wesson et al., 2015). Situated along this highly active convergent margin is the

Laraquete–Carampangue strandplain, a non-deltaic coastal plain of exceptional width (Isla et al., 2023), whose vast progradation contrasts with the limited sediment supply from local coastal basins. This discrepancy led Araya-Cornejo et al. (2025) to propose that strandplain formation was driven not by ordinary sedimentary progradation but by successive Holocene coseismic uplifts generated by predecessor earthquakes analogous to the 2010 event. Each uplift would cause the active beach to be abandoned and a new beach ridge to form, thereby turning the strandplain into a geomorphological archive of past seismicity. Over geological timescales, the continuous preservation of these landforms after successive cycles of tectonic uplift results in the formation of extensive beach-ridge plains or strandplains along convergent coasts globally (McSaveney et al., 2006; Pinegina et al., 2013; Tamura et al., 2007).

While this seismic strandplain-building hypothesis has been inferred from the millennial Holocene stratigraphic record (Araya-Cornejo et al., 2025), direct morphodynamic validation at observable human timescales remains absent. Without a high-resolution modern analogue integrating short-term shoreline dynamics with subsurface architecture, the hypothesis remains geologically plausible but empirically unverified.

The 2010 Maule earthquake (Mw 8.8) provides a uniquely well-constrained modern analogue: it generated significant coseismic coastal uplift directly adjacent to the Laraquete–Carampangue strandplain, enabling a direct, fully integrated observational test of the coseismic beach-ridge formation mechanism inferred from the Holocene stratigraphic record. While prior work has documented post-Maule coastal evolution at decadal timescales (Aedo et al., 2023), no previous study has linked short-term morphodynamics, subsurface radar stratigraphy, and Holocene strandplain architecture at the same site. This study documents the morphodynamic response of Laraquete–Horcones Beach (LHB) to the

2010 coseismic base-level fall through the convergent application of four independent proxies: satellite-derived shoreline analysis (CoastSat–ELTM), multi-temporal seaward dune vegetation line (SVDL) mapping, ground-penetrating radar (GPR) stratigraphy with formal radar-stratigraphic reinterpretation, and UAV–LiDAR topographic differencing, all anchored to the precise temporal datum provided by the earthquake itself.

This study addresses three specific objectives: (1) to quantify the morphological changes and interannual progradation rates of the shoreline and subaerial beach following the 2010 coseismic uplift at LHB; (2) to characterize the beach–aeolian coupling and the morphological and stratigraphic expression of its products, including sand sheets, nebkhas, and incipient beach-ridge sealing, as documented by multi-temporal SVDL mapping, UAV topography, and GPR subsurface architecture; and (3) to link these short- to medium-term morphodynamic responses with the stratigraphic architecture and long-term Holocene evolution of the Laraquete–Carampangue strandplain, evaluating the plausibility of repeated coseismic uplift as the primary mechanism of strandplain construction. While Aedo et al. (2023) documented decadal coastal evolution at adjacent Isla Santa María using geomorphological mapping and satellite imagery, the present study extends that approach by integrating subsurface GPR stratigraphy with surface morphodynamics, establishing dimensional equivalence with the Holocene strandplain inter-ridge architecture, and formalizing the morphodynamic process within a reproducible three-stage conceptual model.

2. Study Area

2.1. Tectonic and Geographic Setting

The study area is located in the coastal zone of the Gulf of Arauco in south-central Chile (37°12′S, 73°13′W). It comprises a beach–aeolian system ~12 km long between the Laraquete and Carampangue rivers, hereinafter referred to as Laraquete–Horcones Beach (LHB; Fig. 1c). Here, the Nazca Plate subducts beneath the South American Plate at ~65 mm yr^{-1} (Jarrin et al., 2022), a setting that favours the recurrence of large megathrust earthquakes. The Gulf of Arauco lies directly above one of the maximum slip patches (~12 m; Fig. 1b) of the 2010 Maule earthquake (Mw 8.8), which had a rupture length of ~500 km and generated significant coseismic coastal uplift of up to ~3 m along the surrounding coast (Kelson et al., 2012). This rupture closely mirrors the spatial distribution and magnitude of the 1835 earthquake (Ms 8.5), during which Charles Darwin documented comparable uplifts of ~2.1 m in the coastal zone of the Gulf of Arauco (Wesson et al., 2015). While instantaneous coseismic uplift drives the sudden progradation of the littoral system, regional morphodynamics are strongly modulated by the full seismic cycle. Following the abrupt uplift, the local coast experiences decades of slow interseismic subsidence, forming a vertical deformation cycle that modulates relative sea level and coastal morphodynamics (Wesson et al., 2015).

Regional GPS data from stations ARCO, PLVP and HLPN confirm that this interseismic subsidence continues at rates of −9.8 to −16.5 mm yr^{-1} more than 15 years after the 2010 event (Supplementary Material S.3, Fig. S5). The complete seismic cycle (instantaneous coseismic uplift followed by decades of interseismic subsidence) produces a net positive vertical displacement over the typical ~100-year recurrence interval. This net tectonic gain allows transient post-seismic morphologies to escape complete marine reworking and become permanently stranded above the active wave base. Each successive cycle thus

153 contributes a preserved beach-ridge and associated aeolian drape to the strandplain
154 architecture, making seismic cycles the building blocks of long-term coastal progradation.
155
156 The active littoral system of the study area, known as LHB, consists of fine-to-medium
157 terrigenous sands sourced mainly from the Carampangue and Laraquete rivers (Fanucci et
158 al., 1992; Gómez et al., 2018). Coastal hydrodynamics are characterized by a microtidal
159 regime (Martínez et al., 2021) and highly energetic southwest swells generated by the
160 Southern Ocean westerlies, with mean significant wave heights of ~2.9 m and peak periods
161 of ~12.8 s (Gómez et al., 2018; Villagrán et al., 2023). Nearshore energy is partially
162 attenuated by wave refraction around the Arauco Peninsula and Santa María Island (Gómez
163 et al., 2018; Villagrán et al., 2023). Predominant southwesterly winds drive localized aeolian
164 transport, and the restricted fluvial sediment input makes the beach morphodynamics highly
165 sensitive to changes in sediment availability rather than to fluvial discharge variability.

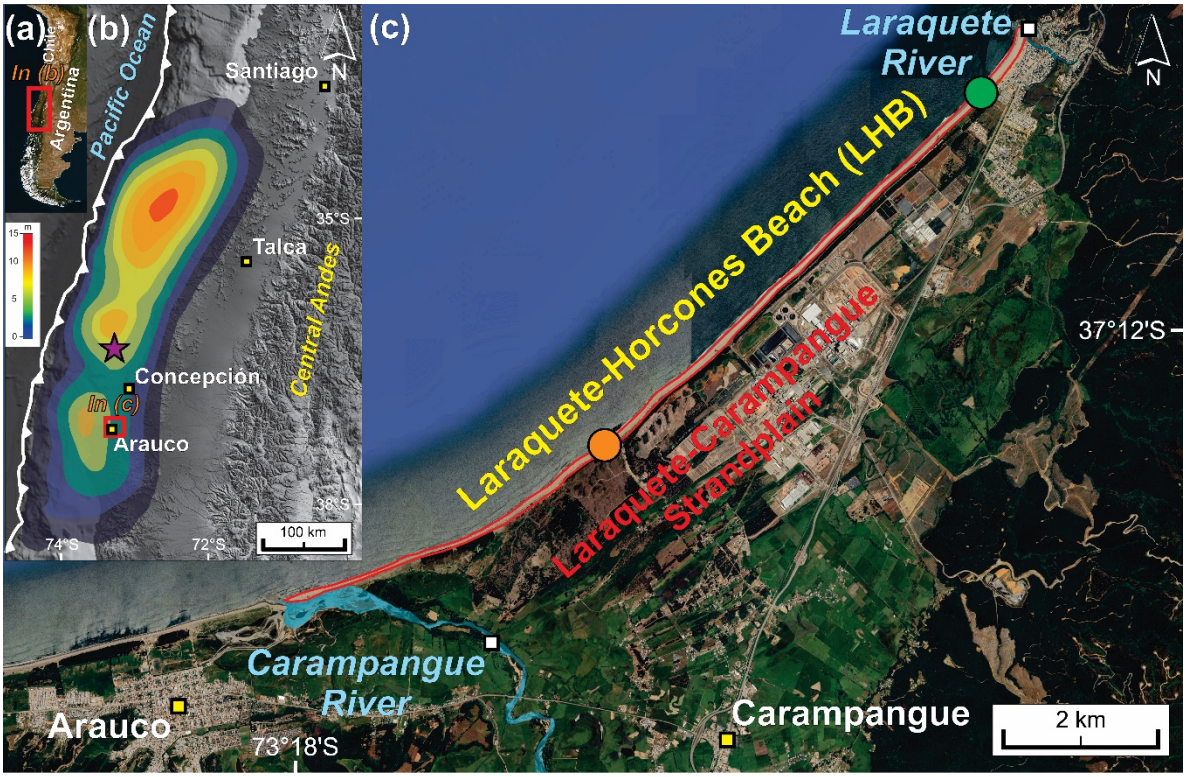

166

Fig. 1. Study area in the context of the rupture zone of the 27 February 2010 Maule earthquake (Mw 8.8). (a) South-central Chile (red rectangle in the left-hand inset). (b) Epicentre (star) and coseismic slip distribution of the 2010 earthquake (modified from Moreno et al., 2010), showing two main high-slip patches (~15 m in the north and ~12 m in the south); the study area is located in front of the southern patch. (c) Laraquete–Horcones beach–aeolian system (red outline) and locations of the ground-penetrating radar profiles GPR 1 (NE zone, green dot) and GPR 2 (SW zone, orange dot).

2.2. Geomorphological Setting

Developed along this active tectonic margin is the Laraquete–Carampangue strandplain, a non-deltaic coastal plain (Isla et al., 2023) of exceptional cross-shore extent. It is bounded to the west by the Pacific Ocean, to the north by the Laraquete River, to the east by a relict marine terrace expressed as a fossil cliff, and to the south by the floodplain of the Carampangue River. Its morphology is defined by a sequence of 52 parallel beach ridges (51 pre-2010 plus one incipient post-2010 ridge documented in this study) consistently oriented parallel to the present shoreline (NW–SE), interspersed with swales and incised by paleochannels that reflect past phases of fluvial dominance (Fig. 2).

The extensive progradation of the plain relative to the limited local sediment supply supports the hypothesis that strandplain formation was driven by successive coseismic uplifts rather than by excess sediment supply (Araya-Cornejo et al., 2025). The present study examines the most recent analogue of this process through a new, high-resolution geomorphological map (Fig. 2) derived entirely from the 1 m LiDAR DTM.

The spatial arrangement of the morphological units relevant to this study is shown in Fig. 2. Fronting the ocean, the modern active beach forms a narrow strip of subaerial sand

representing the post-2010 equilibrium surface. Immediately landward, a continuous mantle of aeolian sand sheets drapes the most recent beach ridges. These sand sheets differ fundamentally from classic foredune systems: they exhibit low relief, lack slipfaces, and show no shore-connected evolutionary continuum (e.g., from incipient to established foredunes). Instead, discrete dune-like accumulations are restricted to isolated nebkhas, reflecting the limited aeolian sediment budget of this coast south of the Biobío River (Araya-Cornejo et al., 2025). Their stabilized, vegetated character makes them effective agents of paleobeach preservation rather than active sites of sediment reworking.

Further inland, the strandplain body is partly overlain by a relict dune field (~5.3 km²). The parabolic morphology and orientation of these dunes indicate that sediment was deflated directly from the Carampangue River, decoupling their formation from classic beach–dune interaction and bypassing the shoreline entirely. Historical records suggest that this field reached its maximum development during the 19th century (Albert, 1900) and has since remained stable. The eastern margin of the system is defined by the fossil cliff of the Holocene marine terrace, marking the pre-Holocene limit of coastal progradation. The low-lying areas between and beyond the strandplain ridges correspond to a floodplain punctuated by oxbow lakes, reflecting a complex history of lateral channel migration and episodic tectonic subsidence and uplift.

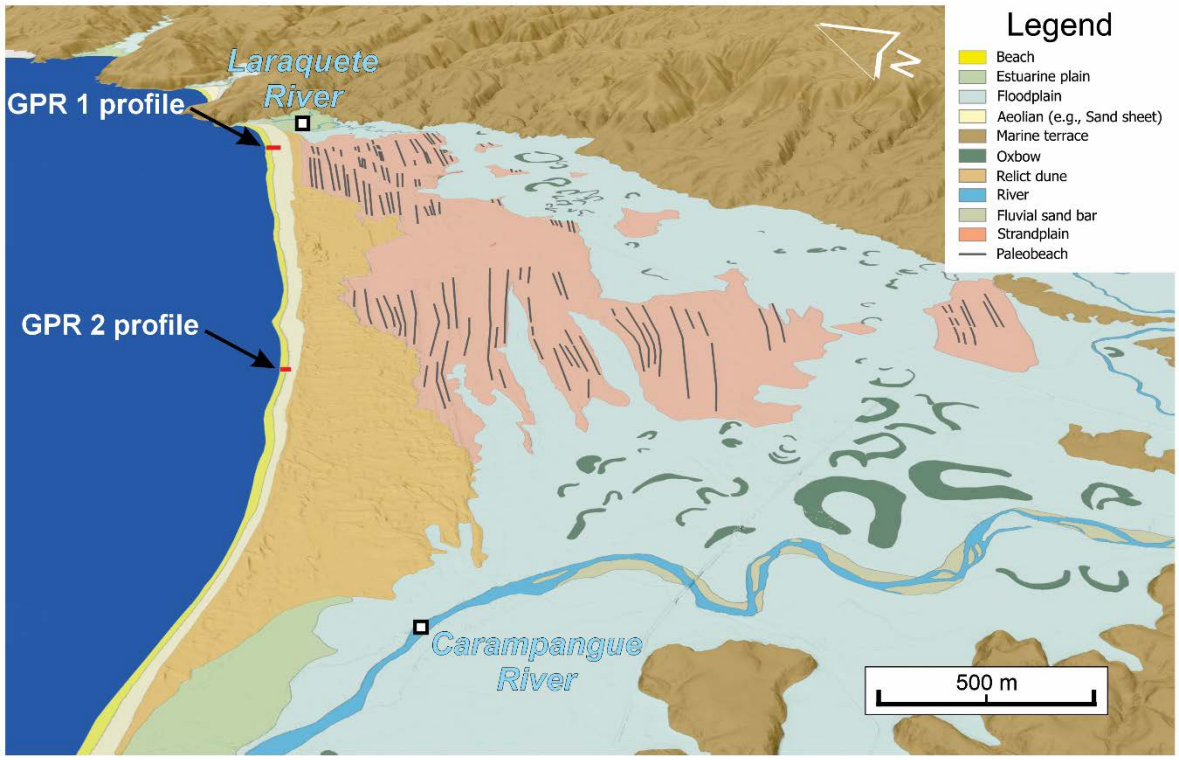

Fig. 2. Geomorphological map of the study area derived from a 1 m resolution Digital Terrain Model (DTM) obtained from airborne LiDAR data. LHB is situated at the western margin of a mixed-origin coastal plain comprising a Holocene strandplain partially incised by fluvial activity, evidenced by a floodplain with active channels and oxbow lakes; and a relict dune field sourced directly by aeolian deflation from the Carampangue River, bypassing the shoreline entirely. Red marks indicate the locations of GPR profiles 1 (Fig. 6) and 2 (Fig. 7) in the NE and SW, respectively.

3. Materials and methods

3.1. Geomorphological base data and LiDAR DTM

The geomorphological map (Fig. 2) was derived from a 1 m resolution bare-earth Digital Terrain Model (DTM) obtained from airborne LiDAR data acquired between 2004 and 2007 by Digimapas Chile. The DTM was reprocessed using post-2010 earthquake GPS

benchmarks referenced to the EGM2008 geoid following the procedure described in Melnick et al. (2026). Morphological units were digitized manually in QGIS 3.x using hillshade derivatives, slope maps, and contour analysis, cross-validated against Google Earth and Esri World Imagery high-resolution orthophotography. All spatial analyses are projected in UTM Zone 18S (EPSG:32718). The LiDAR DTM constitutes the pre-seismic topographic baseline for shore-normal profile comparison (Section 3.5) and for inter-ridge spacing analysis (Supplementary Material S.2).

Inter-ridge spacing of the Laraquete–Carampangue strandplain was quantified from the same LiDAR DTM as the minimum geometric distance between 122 consecutive beach ridge polyline pairs, ordered from seaward to landward by PCA of centroid coordinates. Full details of the distance calculation, ridge ordering procedure, and exclusion criteria are provided in Supplementary Material S.2. Briefly, 87 of 122 consecutive ridge pairs (71.3%) were excluded because they represent inter-patch digitization gaps between laterally discontinuous ridge segments rather than true cross-shore inter-ridge distances; the 100 m threshold was selected to fully separate the two populations visible in the raw bimodal distribution (Supplementary Material S.2, Fig. S4), while retaining all values consistent with the known post-seismic progradation scale (~45–48 m).

3.2. Multi-temporal imagery acquisition, preprocessing, and SVDL mapping

A multi-source, multi-temporal dataset of 11 epochs (2002–2025) was compiled to map the SVDL across the NE and SW sectors (Table 1). For ten epochs, high-resolution imagery was sourced from Google Earth Pro (Google LLC, 2024), attributed to Maxar Technologies WorldView/GeoEye (2002–2019) and CNES/Airbus Pleiades (2021–2023); a conservative working resolution of 0.5 m GSD is adopted for all scenes. The 2025 epoch was acquired

by UAV (Section 3.5). Images were preferentially selected from the austral spring–summer window (October–March; DaSilva et al., 2021); two exceptions apply: (1) the 2010 epoch (Skyfi, 0.48 m GSD, 40 days post-earthquake) establishes the post-seismic morphological baseline, and (2) the 2023 SW-sector image is an early-autumn acquisition retained for temporal continuity.

All datasets were co-registered to WGS84 UTM Zone 18S (EPSG:32718) in ArcGIS Pro (ESRI, 2023). Google Earth Pro scenes were validated against stable reference features (RMSE ≤ 1 pixel); the Skyfi image was validated against GCPs from adjacent epochs (RMSE = 0.48 m). The SVDL was defined as the seaward limit of continuous pioneer macrophyte cover on the windward foredune face (Boak and Turner, 2005) and manually digitized at a fixed scale of 1:2,000 by a single operator, identifying the vegetation–sand boundary from tonal, chromatic, and textural image contrast (DaSilva et al., 2021; Smyth et al., 2022). Ambiguous boundary segments caused by sparse cover, fresh aeolian deposition, or shadow were excluded from analysis.

3.3. Shoreline change statistics and positional uncertainty

Shoreline change statistics were computed with a custom Python script implementing a transect-based workflow equivalent to DSAS (Himmelstoss et al., 2018), using geopandas, shapely, and scipy.stats. Two transect configurations were used: (i) for the CoastSat-derived shoreline analysis (Fig. 3a), shore-perpendicular transects spaced at 50 m along the full LHB littoral cell (~12 km); and (ii) for the high-resolution SVDL analysis at the GPR sectors (Fig. 5; Table 1), denser transects spaced at 15 m within each zone, yielding 24 transects in the NE (~360 m of coast) and 34 in the SW (~510 m of coast). All transects use a length of 100 m extending shoreward from the 2002 baseline. Three statistics were calculated per

transect for the full period (2002–2025), and additionally for the pre-seismic (2002–2010) and post-seismic (2010–2025) sub-periods: Net Shoreline Movement (NSM, m), End Point Rate (EPR, m yr^{-1}), and Linear Regression Rate (LRR ± SE, m yr^{-1}) by OLS regression (minimum 3 observations; SE and R^2 are reported only where this criterion is met; Crowell et al., 1997).

Composite positional uncertainty was estimated following Hapke et al. (2010) as:

$$U_t = \sqrt{U_g^2 + U_d^2}$$

where U_g is image georeferencing uncertainty (0.5 m for Google Earth Pro; 0.48 m for Skyfi; 0.05 m for UAV) and U_d is digitization uncertainty quantified by comparison between independent check digitizations of representative SVDL segments. The 2023 SW-sector epoch carries additional seasonal uncertainty from its early-autumn acquisition date, acknowledged in the interpretation of results.

3.4. Satellite-derived shoreline time series (CoastSat–ELTM)

A continuous satellite-derived shoreline time series was extracted at Laraquete–Horcones Beach (LHB) for the period 2000–2024 using the CoastSat toolkit (Vos et al., 2019). The method retrieves Landsat and Sentinel-2 imagery through Google Earth Engine and maps the instantaneous sand–water interface by supervised classification combined with sub-pixel MNDWI segmentation (typical accuracy ±10 m). All shoreline positions were corrected to a common mean sea level datum using instantaneous tidal levels from the TPXO9 global model (Egbert and Erofeeva, 2002) and the local beach-face slope, thereby minimizing tidal aliasing caused by satellite overpass timing. The coseismic shoreline response was isolated by fitting the Extended Linear Trajectory Model (ELTM; Bevis and Brown, 2014) to the tidally

corrected series. The ELTM decomposes shoreline position into a long-term linear trend, an annual harmonic, and a Heaviside step function that quantifies abrupt displacements; a post-seismic logarithmic relaxation timescale of 0.1 yr was incorporated following the trajectory decomposition framework of Bevis and Brown (2014).

The ±4.9 m uncertainty reported for the coseismic displacement represents the standard error of the Heaviside component from the ELTM fit, and is distinct from the ±10 m positional accuracy of individual CoastSat shoreline detections.

3.5. UAV survey and topographic profile comparison

A UAV survey was conducted on 9 October 2025 using a DJI Phantom 4 RTK (SZ DJI Technology Co. Ltd.) equipped with an FC6310R camera (focal length 8.8 mm; 5,472 × 3,648 px), yielding a GSD of 0.05 m. Imagery was processed in Agisoft Metashape Professional v. 2.2.2 (Agisoft LLC, Russia) following a standard SfM–MVS photogrammetric workflow. Horizontal georeferencing relied on embedded RTK-GNSS coordinates (positional uncertainty ≤ 0.05 m); vertical accuracy was independently constrained using five GCPs extracted from the LiDAR DTM at geomorphologically stable surfaces unaffected by post-seismic change, ensuring datum consistency with the EGM2008 reference (Melnick et al., 2026). Along-shore normal profiles were extracted from both the pre-seismic LiDAR DTM and the post-seismic UAV DTM at the GPR 1 and GPR 2 transect locations (Sections 3.6, 4.3). The seaward terminus of each UAV profile corresponds to the instantaneous waterline at the time of survey; tidal stage during acquisition (10:17–10:34 local time) was 0.15–0.24 m a.s.l. EGM2008, estimated by cosine interpolation from SHOA (2025) tidal predictions at Lebu station. The horizontal uncertainty introduced by tidal variability during the 17-minute survey window is ≤ 8 m, estimated from the characteristic beach-face slope.

3.6. Ground-penetrating radar (GPR) acquisition and radar stratigraphy

GPR data were acquired in 2023 using a GSSI UtilityScan system (Geophysical Survey Systems Inc., Nashua, NH, USA) with a 350 MHz shielded, ground-coupled antenna (wave velocity: 0.15 m ns^{-1}, validated by pit excavation to ≤ 5% depth error; Araya-Cornejo et al., 2025). Raw radargrams were post-processed in RADAN 7 and MatGPR R3 applying de-wow, zero-time correction, horizontal background removal, bandpass filtering, and topographic correction using an Emlid Reach RS2+ DGPS.

GPR 1 (NE zone, 400 m) and GPR 2 (SW zone, 75 m) were first reported by Araya-Cornejo et al. (2025). The present study applies an entirely new radar-stratigraphic framework to the same raw profiles; the scope of reinterpretation and data reuse are detailed in Section 4.2.

3.7. MSAVI2 vegetation dynamics

Vegetation dynamics along both GPR transects were independently characterized using the Modified Soil-Adjusted Vegetation Index 2 (MSAVI2; Qi et al., 1994), computed from annual median composites of Landsat Collection 2 Surface Reflectance imagery (2002–2014) and Sentinel-2 MSI (S2SRHARMONIZED; 2015–2025) processed in Google Earth Engine (Gorelick et al., 2017). MSAVI2 was preferred over NDVI because its adaptive soil-correction factor minimizes the effect of bare sandy substrate on the vegetation signal under sparse pioneer cover (Medina Machín et al., 2019; Qi et al., 1994). Cross-sensor consistency at the 2015 Landsat-to-Sentinel-2 transition was confirmed by Mann-Whitney U test ($p = 1.0$). Temporal trends were assessed by the Mann-Kendall test and Pettitt change-point detection

(Pettitt, 1979). Full details of image preprocessing, index selection, spatial sampling, and statistical parameters are provided in Supplementary Material S.1.

4. Results

4.1. Shoreline evolution derived from satellite images

4.1.1. Coseismic shoreline response and spatiotemporal evolution

Long-term shoreline change rates (Fig. 3a) establish the background morphodynamic state of LHB. The dominant condition across most of the study area corresponded to moderate erosion rates (ranging between −1.5 and −0.2 m yr^{-1}), interrupted by a localized hotspot of intense erosion in the central sector (rates < −1.5 m yr^{-1}); this anomaly may reflect along-strike variability in coseismic slip and associated differential crustal uplift, resulting in locally reduced base-level fall relative to adjacent sectors. The system transitions toward sustained net progradation (> +1.5 m yr^{-1}) at the southwestern limit. This regional erosional trend confirms the sediment-starved background state of LHB, against which the 2010 event stands as the primary driver of mid-term morphodynamic evolution.

The temporal analysis (Fig. 3b) applies the ELTM (Bevis and Brown, 2014), which decomposes the shoreline series into a long-term trend, a seasonal oscillation, and a step-change component, isolating the coseismic signal from background variability. During the pre-seismic period (2000–2010), the shoreline oscillated seasonally around a mean position of approximately −15 m relative to the reference datum, with no discernible net secular trend and a wide uncertainty envelope consistent with the lower density of observations available

prior to 2010. Coinciding with the earthquake on 27 February 2010, the ELTM quantifies an abrupt coseismic seaward displacement of 25 ± 4.9 m, accurately captured by the model's Heaviside step-function component. This abrupt accretion shifted the beach baseline. During the post-seismic period (2010–2024), the shoreline stabilized around a new positive baseline ranging from +5 to +20 m. While sustaining seasonal oscillations of comparable amplitude to the preceding period, this new morphological state is characterized by a markedly narrower uncertainty envelope, reflecting a substantially greater density of available imagery. The system's current configuration is thus primarily a legacy of the 2010 coseismic advance.

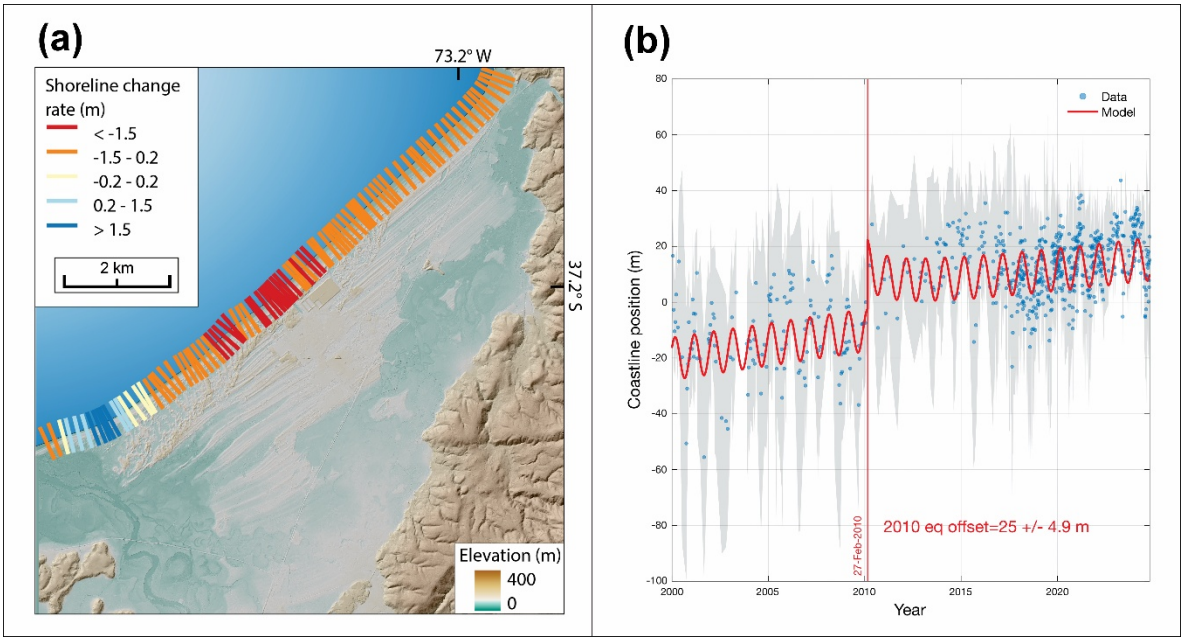

Fig. 3. Spatial and temporal characterization of shoreline dynamics at the LHB. (a) Long-term shoreline change rates (m yr^{-1}) derived from shore-perpendicular transects at 50-m intervals, quantified by least-squares regression through all satellite-derived shoreline positions. Rate categories: intense erosion (< −1.5 m yr^{-1}), moderate erosion (−1.5 to −0.2 m yr^{-1}), stability (−0.2 to 0.2 m yr^{-1}), moderate accretion (0.2 to 1.5 m yr^{-1-1}), and sustained progradation (> +1.5 m yr^{-1}); background hillshade derived from a 1 m resolution LiDAR-derived DTM. (b) Satellite-derived shoreline position time series at LHB (2000–2024; CoastSat, Vos et al., 2019), tidally corrected using the TPXO9 global tidal model (Egbert and Erofeeva, 2002). Blue circles: individual observations; grey

shading: 95% confidence envelope. The red curve shows the best-fit Extended Linear Trajectory Model (ELTM; Bevis and Brown, 2014). The vertical red line marks the Mw 8.8 Maule earthquake (27 February 2010); the Heaviside component quantifies the coseismic shoreline displacement at 25 ± 4.9 m.

4.1.2. Pre- and post-seismic coastal progradation assessed from the seaward dune vegetation line (SVDL)

Figure 4 maps the multi-temporal SVDL (2002–2025) in two representative sectors of the LHB system: the NE sector (Fig. 4a) in the northern/central half and the SW sector (Fig. 4b) in the southern half, both co-located with GPR 1 and GPR 2. This selection enables direct correlation between surface progradation rates and subsurface stratigraphy (Section 4.2). Both sectors show a net seaward advance, with closely spaced pre-2010 lines contrasting with broader post-2010 spacing. SVDL positions were digitized to compute NSM, EPR, and LRR.

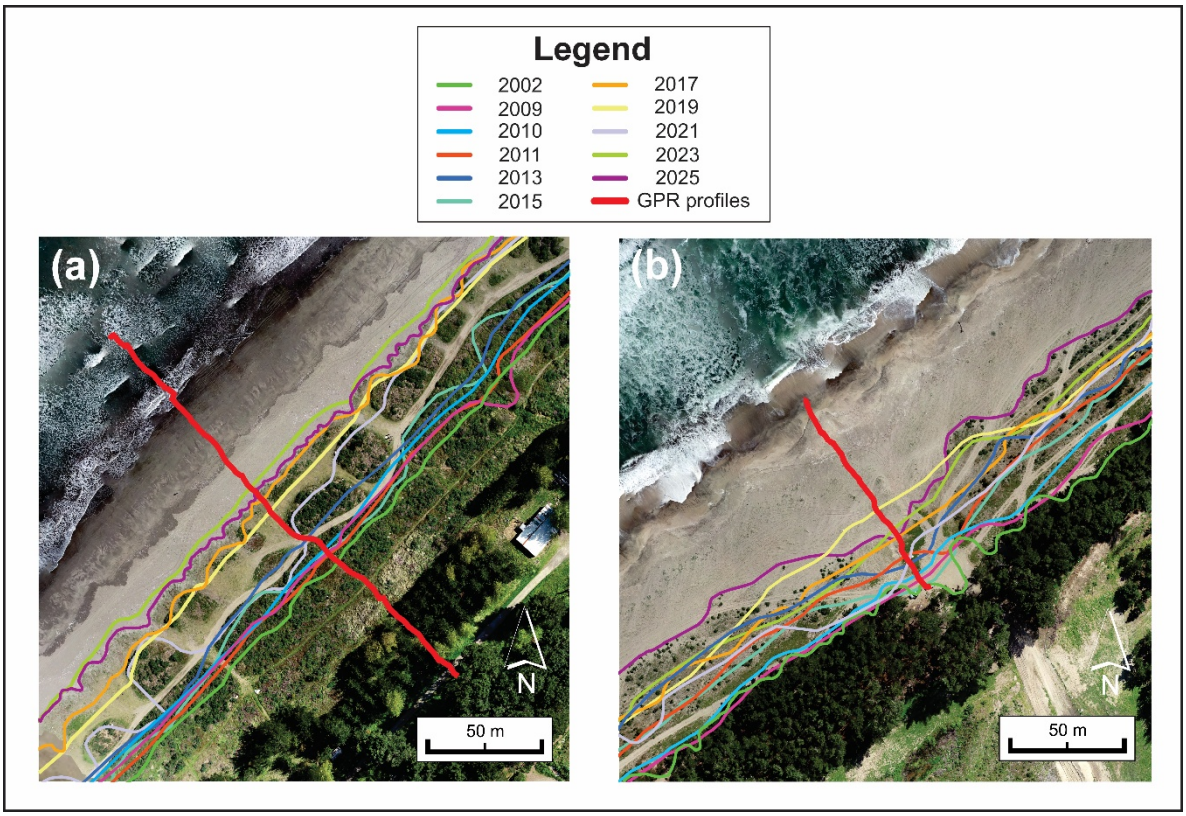

Fig. 4. Multi-temporal spatial distribution of the seaward dune vegetation line (SVDL) mapped between 2002 and 2025, overlaid on high-resolution orthophotography. (a) NE zone and (b) SW zone. Coloured lines show multi-temporal SVDL positions; net seaward advance is documented across the 23-year record, though individual epoch positions exhibit interannual variability that is most pronounced in the SW zone. The 2002 line serves as the reference baseline. Red solid lines denote the GPR profile locations (GPR 1 and GPR 2).

During the pre-seismic period (2002–2010), cross-shore displacement was limited in both zones (NSM = 8.4 ± 1.6 m in NE; 12.9 ± 10.9 m in SW; EPR ≈ 1.1–1.6 m yr^{-1}; full statistics in Table 1). The substantially higher standard deviation in the SW zone reflects greater spatial heterogeneity among transects, while the near-parallel 2002–2010 lines in the NE zone (Fig. 4a; Fig. 5a) indicate low interannual variability prior to the earthquake.

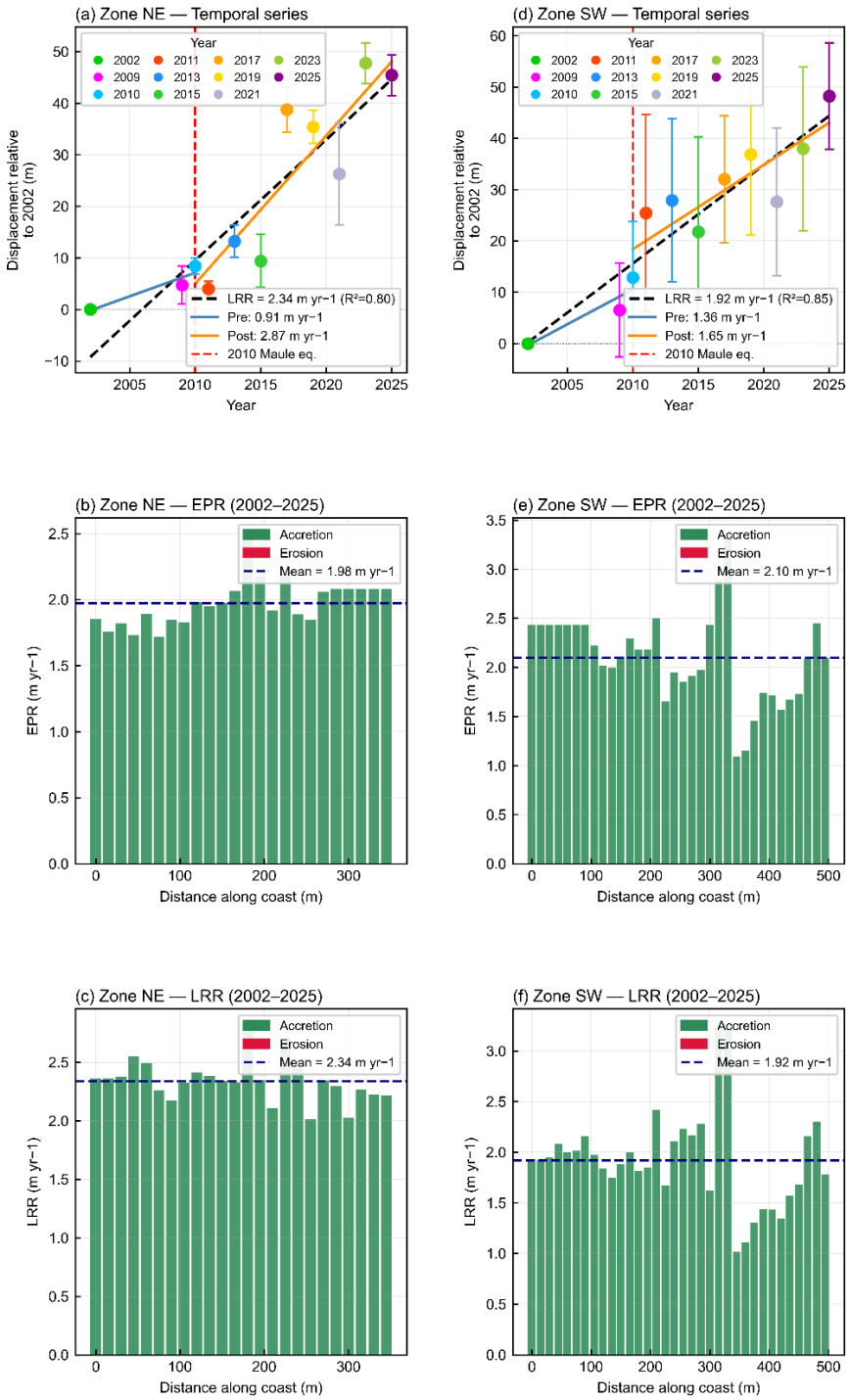

Fig. 5. Spatiotemporal analysis of seaward dune vegetation line (SVDL) displacement (2002–2025). Panels (a–c) represent the NE sector, and panels (d–f) represent the SW sector. (a, d) Temporal series of SVDL displacement relative to the 2002 baseline; coloured circles denote individual epochs (mean ± 1σ across transects), and linear fits show pre-seismic, post-seismic, and total-period LRRs

(legend in each panel). (b, e) Along-shore distribution of End Point Rates (EPR) by transect for the full study period (2002–2025). (c, f) Along-shore distribution of Linear Regression Rates (LRR) by transect for the full study period. Pre-seismic LRR values reported in Table 1 rest on only two SVDL observations and should be interpreted with caution (see footnote to Table 1).

Sustained seaward progradation of the SVDL is recorded in both zones from 2010–2011 onward (Fig. 4a, b; Fig. 5a, d). Post-seismic NSM (2010–2025) ranges from ~35 to ~37 m and total NSM (2002–2025) from ~45 to ~48 m, with corresponding two- to threefold increases in EPR and LRR relative to the pre-seismic period (full statistics in Table 1).

Table 1. Summary of shoreline change statistics (NSM, EPR, and LRR) for the seaward dune vegetation line (SVDL) in the NE and SW zones. Rates are calculated for the pre-seismic (2002–2010), post-seismic (2010–2025), and total study periods (2002–2025).

Zone	Period	NSM (m)	σ NSM (m)	EPR (m yr^{-1})	LRR ± SE (m yr^{-1})*	R2
NE	Pre-seismic (2002–2010)	8.41	± 1.57	1.05	0.91†	—
NE	Post-seismic (2010–2025)	37.01	± 4.18	2.47	2.87 ± 0.55	0.80
NE	Total (2002–2025)	45.43	± 3.96	1.98	2.34 ± 0.39	0.80
SW	Pre-seismic (2002–2010)	12.85	± 10.93	1.61	1.36†	—
SW	Post-seismic (2010–2025)	35.37	± 11.25	2.36	1.65 ± 0.38	0.73
SW	Total (2002–2025)	48.22	± 10.42	2.10	1.92 ± 0.27	0.85

* LRR computed by OLS regression on zone-mean SVDL positions per epoch; SE and R^2 reported only where ≥ 3 epochs are available (post-seismic and total periods).

† Pre-seismic LRR is based on two SVDL epochs only (2002 and April 2010); SE and R^2 are not reported as they carry no statistical meaning with zero degrees of freedom. EPR constitutes the primary metric for characterizing pre-seismic background behaviour.

The SW zone exhibits a markedly more dynamic spatial pattern than the NE zone (Fig. 5e, f). The larger transect-to-transect variability in the SW zone (σ NSM: ±10.42 m vs. ±3.96 m in the NE zone) indicates a heterogeneous geomorphological response along the coast. No transect records net landward displacement (Fig. 5b, c, e, f). In the SW zone, localized EPR peaks exceeding 3.0 m $yr^{-1}$and LRR peaks exceeding 4.0 m yr^{-1}occur at approximately 300 m and 500 m along the coast (Fig. 5e, f), indicating sectors of particularly rapid vegetation advance. In the NE zone, the 2023–2025 lines converge toward a stabilized position, with reduced cross-shore spacing relative to the 2017 line (Fig. 4a). Conversely, in the SW zone, the 2025 line occupies the most seaward position in the entire 23-year record (Fig. 4b). The early-autumn acquisition of the 2023 SW-sector image may introduce a slight landward bias in that epoch's SVDL position relative to spring–summer acquisitions.

MSAVI2 analysis of Landsat/Sentinel-2 imagery (2002–2025) independently corroborates progressive seaward vegetation colonization in the NE zone from 2014 onward (Pettitt structural change-point test, $p < 0.0001$, one year before the Landsat-to-Sentinel-2 sensor transition; Mann-Kendall $\tau = 0.821$, $p < 0.0001$ on the Landsat-only period), spatially concentrated in the 0–90 m sector closest to the shoreline (Supplementary Material S.1, Fig. S1). No equivalent trend was detected at the SW zone (Mann-Kendall $\tau = 0.077$, $p = 0.76$), a null result interpreted as ecologically consistent with the narrower aeolian sand sheet and the structural absence of an interior vegetation reservoir at that site (Fig. S3C,

Supplementary Material S.1). This absence of MSAVI2 signal does not imply an absence of geomorphological response; rather, it reflects a spectrally weaker vegetation signal under sparser pioneer cover, consistent with the sustained SVDL progradation documented in that sector (Table 1).

4.2. Subsurface stratigraphy of pre- and post-seismic beach sequences derived from GPR

Data reuse and novelty statement. The raw GPR radargrams of profiles GPR 1 and GPR 2 were originally acquired and reported by Araya-Cornejo et al. (2025) in the context of millennial-scale strandplain evolution. The present study does not reinterpret those data for the same purpose; rather, it applies an entirely new analytical framework to the same raw profiles. Specifically, all elements presented here are original to this study: (1) the formal four-facies radar-stratigraphic classification scheme (PBF, BBF, RCF, AF; Table 2), which was not used in Araya-Cornejo et al. (2025); (2) the spatial correlation of subsurface radar facies with the multi-temporal SVDL positions from the 2002–2025 satellite record, which provides an independent surface chronological constraint absent from the prior study; and (3) the topographic comparison between the pre-seismic LiDAR DTM and the post-seismic UAV DTM acquired in October 2025, a dataset that did not exist at the time of the earlier publication. The reuse of raw GPR data is explicitly analogous to the reanalysis of existing borehole or seismic-reflection datasets under a new interpretive framework, a standard practice in stratigraphic research.

GPR 1 (NE zone, 400 m) and GPR 2 (SW zone, 75 m) are located shore-normal at the same transects as the SVDL analysis (Section 4.1.2; Fig. 1c). Both radargrams are reinterpreted here using a formal radar-stratigraphy approach (Mitchum et al., 1977; Neal, 2004); the four-

497 facies classification and three-component reflector notation are detailed in Section 3. While
498 the temporal assignment of the subsurface units lacks absolute chronological dating, their
499 interpretation is robustly constrained by spatial correlation with the SVDL positions from the
500 2002 satellite record.

501

502 **Table 2.** Radar facies identified in GPR 1 (Fig. 6) and GPR 2 (Fig. 7), their dominant reflector
503 characteristics, and associated depositional context. LWD reflectors are exclusive to GPR 1.

Radar facies	Dominant reflector characteristics	Depositional context
PBF – Prograding Beach Facies	C–MA–SWD; C–HA–SWD; MC–MA–SWD; MC–HA–SWD	Foreshore clinoforms; systematic seaward dip records the advancing beachface
BBF – Berm Beach Facies	MC–HA–H; MC–MA–H; MC–MA–CXU; MC–HA–CXU; MC–LA–CXU; MC–HA/MA–LWD*	Berm crest and upper berm deposits; convex-up geometry mirrors arched berm morphology; LWD* (GPR 1 only)
RCF – Runnel Channel Facies	MC–MA–CU; MC–LA–CU	Runnel fill; concave-up geometry reflects bowl-shaped channel morphology
AF – Aeolian Facies	D–LA–W; D–MA–W	Aeolian sand sheet; discontinuous, low-amplitude, wavy reflectors lacking organized marine bedding

504

505 4.2.1. NE Zone — GPR 1

506

507 The raw radargram (Fig. 6a) covers the first ~175 m of the 400 m profile, over an elevation
508 range of −3 to +3 m a.s.l. A zone of signal attenuation extends from 0 to approximately 25
509 m, associated with high electromagnetic conductivity in the saturated nearshore sediments.
510 Interpretable reflectors begin at approximately 25 m, coinciding with the position of the

current beach ridge identified from satellite imagery analysis (Fig. 4a), and extend to the landward end of the profile.

The current beach zone (~50–100 m) shows MC–HA–H and MC–MA–CXU reflectors at berm crests (~55 m and ~75 m) underlain by SWD foreshore clinoforms; a CU package at ~70 m records the active runnel. The pre-earthquake zone (~100–150 m) replicates this architecture at greater depth, with additional localized LWD reflectors absent from the current zone (Fig. 6b).

Panel (c) assigns each package to the radar facies (Table 2). The BBF is identified at the active berm crest positions (~55 m and ~75 m) and at their buried pre-earthquake equivalents (~100–150 m). In both the current and pre-earthquake cycles, BBF directly overlies a PBF package, constituting the vertical succession PBF → BBF. The RCF is identified at the current runnel (~70 m) and at the pre-earthquake runnel (~118 m). The AF occupies the upper portion of the profile landward of approximately 150 m, capping both the pre-earthquake and ancient beach structures.

Panel (d) defines four stratigraphic bodies (Fig. 6d). The current beach facies (light blue) extends from ~50 m to the current vegetation line (~93 m; Fig. 4a), spanning ~43 m. The pre-2010 earthquake beach facies (medium blue) spans ~70–155 m, bounded landward by the pre-2010 SVDL position recorded in the 2002 dataset (~143 m; Fig. 4a). The ancient beach facies (dark blue/grey) occupies the deepest and most landward levels of the profile. The aeolian facies (yellow) drapes the surface from approximately 100 m to the landward limit of the profile, increasing in thickness inland.

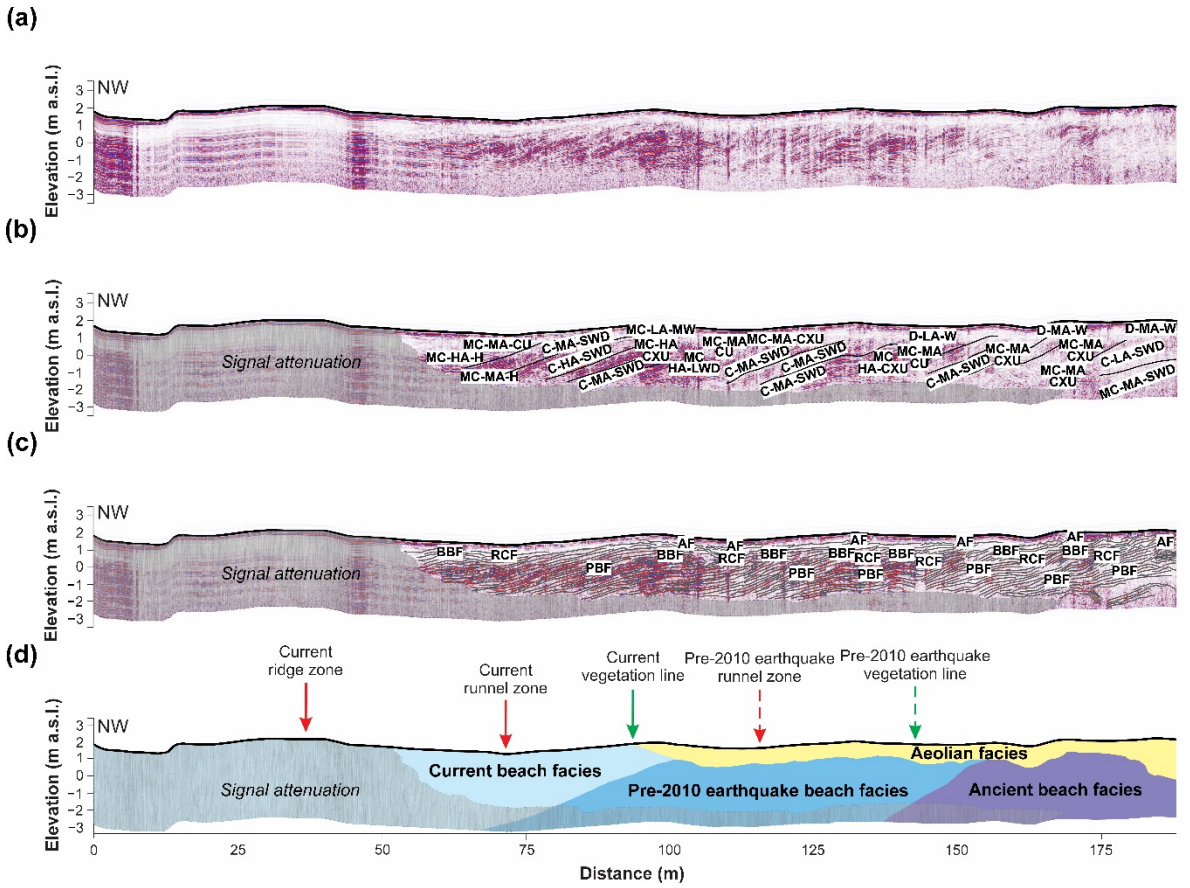

535

536 **Fig. 6.** GPR 1 profile acquired in the NE zone (location in Fig. 1c). (a) Raw, topographically corrected
537 radargram; NW end (active beach) at left; horizontal axis in meters, vertical axis in m a.s.l.; hatched
538 zone (0–~25 m) denotes nearshore signal attenuation. (b) Reflector characterization using the three-
539 component notation of Table 2, after Neal (2004) and Mitchum et al. (1977). (c) Radar facies (see
540 Table 2). Solid black lines represent radar bounding surfaces separating distinct facies. (d) Color-
541 coded stratigraphic units: current beach facies (light blue), pre-2010 earthquake beach facies
542 (medium blue), ancient beach facies (dark blue/grey), aeolian facies (yellow). Surface
543 geomorphological markers are indicated at the top of the panel (red arrows: morphological ridges and
544 runnels; green arrows: vegetation lines): current beach ridge zone (~25 m), current runnel zone (~75
545 m), and current vegetation line (~100 m), identified from satellite imagery analysis (Fig. 4a); pre-2010
546 earthquake runnel zone (~125 m) and pre-2010 earthquake vegetation line (~150 m), derived from
547 the 2002 shoreline record of the SVDL analysis (Fig. 4a). Panels (b)–(d) represent a new radar-
548 stratigraphic interpretation developed in the present study, adapted from Araya-Cornejo et al. (2025),

549 Remote Sensing, 17, 2798 (CC BY 4.0; https://doi.org/10.3390/rs17162798). Note: the distance axis
550 originates at the seaward (NW) end, where signal attenuation marks the saturated nearshore zone
551 approximately coincident with the 2025 waterline (Fig. 8); distance increases landward.
552
553 4.2.2. SW zone — GPR 2
554
555 The reflector architecture in GPR 2 is structurally analogous to that of GPR 1, although
556 spatially compressed and lacking LWD reflectors. Both profiles show the same diagnostic
557 vertical succession PBF → BBF, locally incised by RCF structures, confirming that the
558 coseismic stratigraphic signature is pervasive across both zones (Fig. 7).
559
560 The raw radargram (Fig. 7a) extends 75 m in the shore-normal direction, with NW at the left
561 margin, over an elevation range of approximately −2 to +6 m a.s.l. A signal attenuation zone
562 is recorded at the NW end of the profile, and interpretable reflectors begin at approximately
563 15 m. Satellite imagery confirms the formation of a new post-earthquake shoreface at
564 approximately 15 m from the NW end of the profile (Araya-Cornejo et al., 2025).
565
566 Translated into depositional facies, panel (c) identifies the same four radar facies as in GPR
567 1. The BBF is present at multiple depth levels across both the current and the pre-
568 earthquake zones, each occurrence directly overlying a PBF package in the succession PBF
569 → BBF. The RCF is identified at the current runnel (~30 m) and at the pre-earthquake runnel
570 (~50–55 m). Scattered AF labels appear at the surface of the landward portion of the profile
571 (>~65 m), recording thin aeolian deposits.
572
573 At the stratigraphic level, panel (d) defines three color-coded units within the 75 m profile
574 (Fig. 7d). The current beach facies (light blue) extends from approximately 15 m to the

current vegetation line at approximately 35–40 m, in a position consistent with the most seaward SVDL mapped at the GPR 2 transect in Fig. 4b. The pre-2010 earthquake beach facies (medium blue) spans approximately 35–70 m, bounded landward by the pre-2010 earthquake vegetation line at approximately 70 m, which corresponds to the earliest SVDL position at this transect in the 2002 shoreline record (Fig. 4b). The ancient beach facies (purple) is present at the deepest levels of the landward portion of the profile. Unlike in GPR 1, no distinct aeolian stratigraphic unit is differentiated in panel (d) of Fig. 7; the AF identified in panel (c) represents a thin surface deposit insufficient to constitute a separate color-coded unit at the scale of this profile.

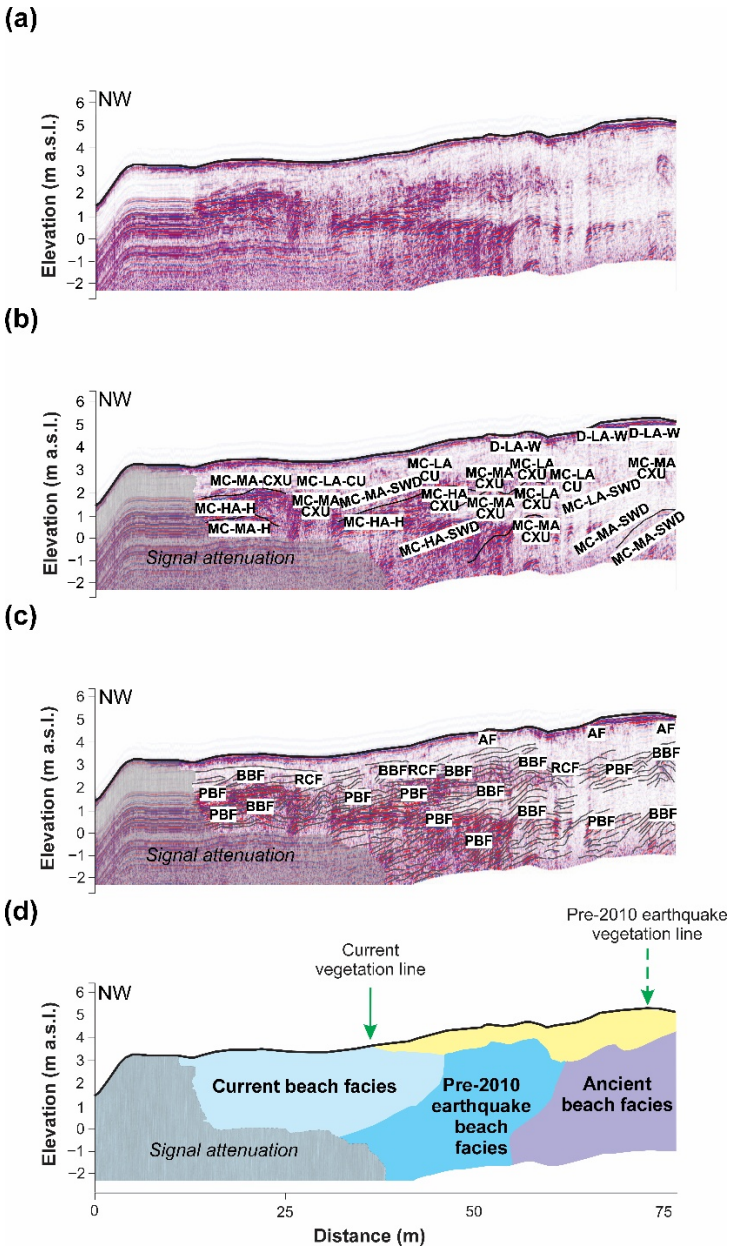

Fig. 7. GPR 2 profile acquired in the SW zone (location in Fig. 1c). (a) Raw, topographically corrected radargram; NW end (active beach) at left; horizontal axis in meters, vertical axis in m a.s.l.; hatched zone (0–~15 m) denotes nearshore signal attenuation. (b) Reflector characterization using the three-component notation of Table 2, after Neal (2004) and Mitchum et al. (1977); LWD reflectors are absent in this profile. (c) Radar facies (see Table 2). Solid black lines represent radar bounding surfaces separating distinct facies. (d) Color-coded stratigraphic units: current beach facies (light blue), pre-2010 earthquake beach facies (medium blue), ancient beach facies (purple). Green arrows indicate the current vegetation line (~35 m) and the pre-2010 earthquake vegetation line (~70 m), derived

from the SVDL analysis (Fig. 4b). No aeolian unit is shown in panel (d); AF deposits are insufficiently thick at this location to constitute a separate stratigraphic body. Panels (b)–(d) represent an extended radar stratigraphy interpretation developed in the present study. Adapted from Araya-Cornejo et al. (2025), Remote Sensing, 17, 2798 (CC BY 4.0; https://doi.org/10.3390/rs17162798). Note: the distance axis originates at the seaward (NW) end, approximately coincident with the 2025 waterline (Fig. 8); distance increases landward.

4.2.3. GPR cross-profile comparison

Both profiles record a consistent spatial asymmetry between the two zones. In the NE zone (Fig. 6d), the current beach facies spans approximately 75 m, whereas in the SW zone (Fig. 7d) both the current and pre-earthquake units are markedly more compressed. This spatial contrast is consistent with the wider post-seismic beach documented in the NE zone by the SVDL analysis (Section 4.1.2, Fig. 4). The PBF → BBF succession, locally incised by RCF structures, constitutes the primary stratigraphic signature of each beach cycle in both profiles. LWD reflectors within the BBF of the pre-earthquake zone are exclusive to GPR 1 (NE zone), representing an additional asymmetry in internal berm architecture not observed in GPR 2 (SW zone).

Additionally, both profiles exhibit an abrupt landward decrease in radar signal amplitude across the boundary between the active post-seismic beach and the older pre-earthquake facies. While recent deposits preserve high-amplitude reflections (e.g., MC-HA-H) reflecting intact primary structures, the ancient and pre-earthquake facies transition sharply into attenuated, medium-to-low amplitude or semi-transparent signatures capped by low-amplitude, sub-horizontal Aeolian Facies (AF), characteristic of structureless sand sheets (Bertran et al., 2020; Rocha et al., 2013).

4.3. Topographic comparison between the pre-seismic LiDAR DTM and the post-seismic UAV DTM

All GPR radargrams (Figs. 6–7) and topographic profiles (Fig. 8) share a common shore-normal axis convention: distance originates at the seaward (NW) end and increases landward. Both datasets follow the same shore-normal transects. The seaward terminus of the GPR profiles corresponds to the saturated nearshore zone (~0–25 m in GPR 1), approximately coincident with the 2025 waterline; interpretable radar facies thus begin near the active berm crest (~1.5–2.0 m a.s.l. in Fig. 8). K-feldspar pIR-IRSL luminescence or radiocarbon dating of the facies boundaries represents a critical target for future work.

Figure 8 compares shore-normal profiles from the pre-seismic LiDAR DTM (Digimapas Chile, 2004–2007; 1 m) and the post-seismic UAV DTM (9 October 2025; 0.05 m) for the NE (Fig. 8a) and SW (Fig. 8b) zones, both referenced to EGM2008. Although the LiDAR DTM predates the earthquake by 3–6 years, pre-seismic SVDL records (Section 4.1.2) document minimal cross-shore displacement (NSM = 8.41 ± 1.57 m over 8 years) and low interannual variability in the NE zone, confirming geomorphological near-stasis during this interval and supporting the use of the LiDAR DTM as a representative pre-seismic topographic baseline. The horizontal offset between the LiDAR (×) and UAV (▼) seaward limits, ~20 m in the NE zone and ~30 m in the SW zone, reflects waterline advance between surveys (terminal symbols defined in Fig. 8). Both profiles follow the same shore-normal transects as GPR 1 and GPR 2 (Section 4.2). Accordingly, cross-shore distances in this section are reported as displacements between identifiable geomorphic markers, specifically the SVDL positions and berm crests visible in both datasets, rather than as absolute positions from the profile origin.

645

646 4.3.1. NE zone

647

648 The pre-seismic LiDAR profile (Fig. 8a, green) begins its seaward data limit at approximately
649 20 m from the profile origin (x = 0), at an elevation of approximately 1.0 m a.s.l. (EGM2008).
650 From this point, the surface rises to a subdued ridge crest at approximately 1.5–1.6 m a.s.l.
651 near 25 m, followed by a broad runnel depression maintained at approximately 1.3–1.5 m
652 a.s.l. between 30 and 75 m. Beyond the runnel, the profile rises to approximately 2.2 m a.s.l.
653 at ~90 m, coinciding with the pre-seismic SVDL position, and maintains stable elevations of
654 2.0–2.2 m a.s.l. toward the landward limit of the transect. This ridge–runnel–SVDL sequence
655 at the surface corresponds to the subsurface architecture of the pre-2010 earthquake beach
656 facies identified in GPR 1 (Section 4.2.1), where buried BBF and RCF structures occupy the
657 100–150 m interval of the GPR 1 distance axis beneath the aeolian-draped surface.

658

659 The post-seismic UAV profile (Fig. 8a, red) begins at the 2025 waterline at x ≈ 0 m and an
660 elevation of approximately 0.6 m a.s.l. The surface rises sharply to a berm crest of
661 approximately 2.1 m a.s.l. by ~50 m, where the current SVDL is located. Landward of the
662 current SVDL, the UAV surface maintains elevations consistently above 2.0 m a.s.l. and is
663 characterized by high-frequency microrelief with amplitudes of approximately 0.1–0.3 m,
664 absent in the smoother LiDAR profile. The UAV surface elevation exceeds the LiDAR
665 surface elevation across their entire shared cross-shore overlap, with a net vertical
666 difference of approximately 0.5–0.8 m.

667

668 The cross-shore displacement between the pre-seismic SVDL (LiDAR, 2004–2007) and the
669 post-seismic SVDL (UAV, 2025), measured along the GPR 1 transect, amounts to
670 approximately 43 m. This value falls within the range defined by the post-seismic NSM

(37.01 ± 4.18 m) and the total NSM (45.43 ± 3.96 m) derived from the multi-transect SVDL satellite analysis for the NE zone (Section 4.1.2; Table 1).

4.3.2. SW zone

The pre-seismic LiDAR profile (Fig. 8b, green) begins at its seaward data limit at approximately 30 m from the profile origin (x = 0), at an elevation of approximately 1.0 m a.s.l., and rises at a consistent gradient to approximately 5.5–5.8 m a.s.l. at 100 m. The berm structure at ~30 m is subdued relative to the NE zone, and a runnel depression comparable to that of the NE profile is not identifiable in the LiDAR surface. The pre-seismic SVDL is located at approximately 95 m from the profile origin (x = 0), at elevations of approximately 5.0–5.5 m a.s.l. This overall steeper and morphologically simpler surface mirrors the more compressed subsurface architecture documented in GPR 2 (Section 4.2.2).

The post-seismic UAV profile (Fig. 8b, red) starts at the 2025 waterline at x ≈ 0 m and an elevation of ~0.4 m a.s.l., rising continuously along a steep gradient to approximately 4.0–4.5 m a.s.l. at the current SVDL at ~73–75 m. The UAV surface in the SW zone is notably smoother than in the NE zone, with high-frequency microrelief largely absent. As in the NE zone, the UAV surface elevation exceeds the LiDAR surface elevation across their shared cross-shore overlap, with a net vertical difference of approximately 0.3–0.6 m.

The cross-shore displacement between the pre-seismic SVDL (LiDAR, 2004–2007) and the post-seismic SVDL (UAV, 2025), measured along the GPR 2 transect, amounts to approximately 21 m. Although the 21 m displacement at the GPR 2 transect is below the zonal average (35.37 ± 11.25 m; Table 1), the profile demonstrates that the diagnostic PBF → BBF succession forms and is preserved even in sectors of restricted accretion. This

confirms that the coseismic stratigraphic reorganization is a systemic feature driven by base-level fall, not an artifact limited to maximum-deposition zones.

4.3.3. Topographic cross-profile comparison

Both zones record a consistent pattern of seaward SVDL displacement and net vertical accretion between the pre-seismic LiDAR and post-seismic UAV surveys. The NE zone documents a broader seaward advance (~43 m), a lower maximum berm elevation (~2.1 m a.s.l.), and a texturally complex UAV surface with high-frequency microrelief. The SW zone records a narrower advance at the GPR 2 transect (~21 m), a higher berm/SVDL elevation (~4.0–4.5 m a.s.l.), and a smoother UAV surface. In both zones, the UAV surface stands 0.3–0.8 m above the LiDAR surface across their shared cross-shore overlap. Vertical co-registration uncertainty between the LiDAR DTM (~0.15 m) and UAV DTM (~0.05 m) yields a combined Minimum Detectable Change of approximately 0.16 m at 1σ; the documented vertical differences (0.3–0.8 m) exceed this threshold by a factor of 2–5, confirming their geomorphological significance. The inter-SVDL displacements identified in the topographic profiles (43 m in the NE zone, 21 m in the SW zone) are consistent with the post-seismic progradation documented by the satellite-based SVDL analysis (Section 4.1.2).

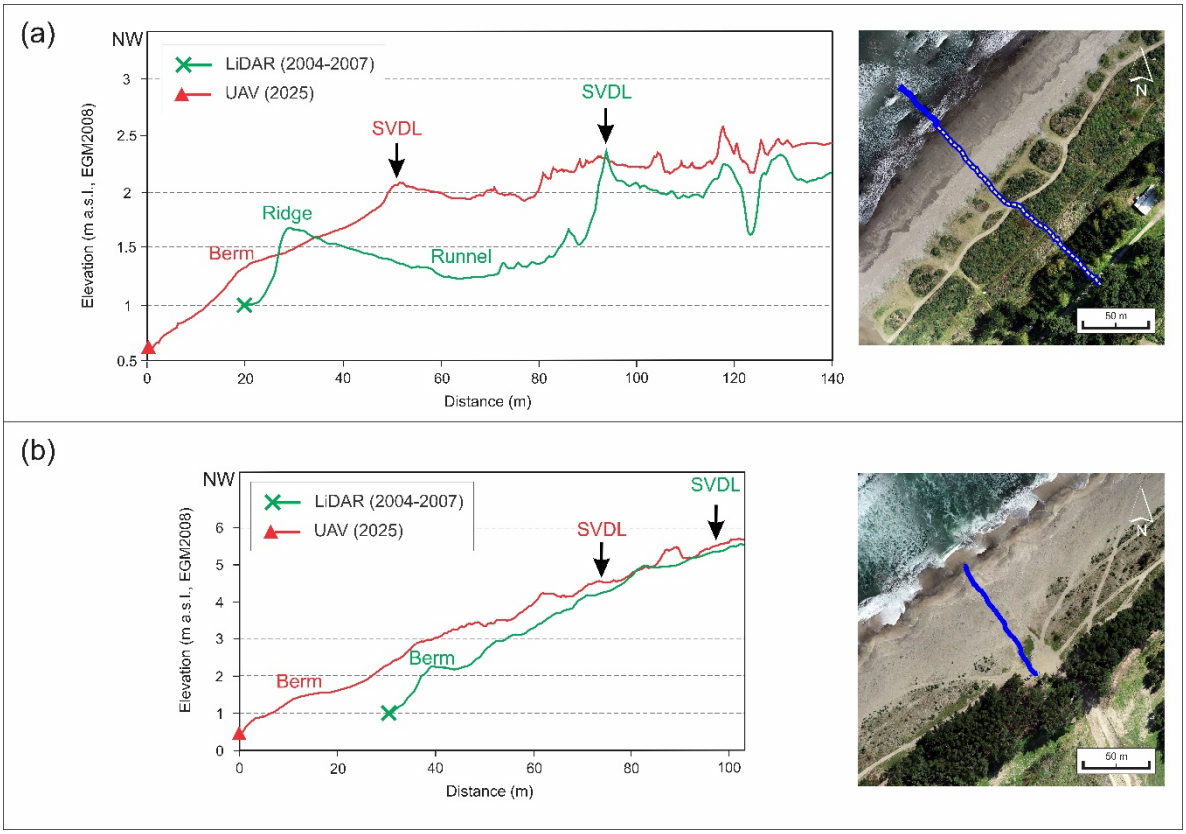

Fig. 8. Shore-normal topographic profiles from the (a) NE and (b) SW sectors, comparing the pre-seismic LiDAR-derived DTM (green; Digimapas Chile, 2004–2007; 1 m resolution) and the post-seismic UAV-derived DTM (red; 9 October 2025; 0.05 m resolution). Both profiles are referenced to the EGM2008 vertical datum using post-2010 earthquake GPS benchmarks (Melnick et al., 2026). Terminal symbols: × LiDAR data limit; ▼ UAV waterline at time of survey (tidal stage +0.15–0.24 m a.s.l.; SHOA, 2025). Right-hand insets show the spatial location of each profile on high-resolution orthophotography. In both panels, the solid blue line indicates the full extent of the GPR survey transect (GPR 1 in (a), GPR 2 in (b); see Fig. 1c). In panel (a), the dashed yellow line delineates the subaerial segment from which the topographic profiles were extracted; the seaward portion of the GPR 1 transect beyond this segment corresponds to the active intertidal and nearshore zone, where neither the LiDAR nor the UAV surveys acquired land-surface data. In panel (b), the GPR 2 transect lies entirely within the subaerial domain, and the full blue line therefore coincides with the profile extent. Distance axis originates at the 2025 waterline (seaward end) and increases landward, matching the convention used in the GPR radargrams (Figs. 6–7). The berm crest visible at ~20–30

m corresponds to the BBF/PBF boundary identified at the seaward end of the interpretable zone in both radargrams.

5. Discussion

5.1. Shoreline response to coseismic uplift in a sediment-starved system

Long-term CoastSat-derived change rates reveal a dominant condition of moderate net erosion across most of the system (−0.2 to −1.5 m yr^{-1}), interrupted by a localized hotspot of intense erosion in the central sector (Fig. 3a). This erosive signature reflects the structurally sediment-starved character of the LHB littoral cell, as quantitatively confirmed by the absence of secular accretionary trend in pre-seismic CoastSat records (Section 4.1.1), where fluvial input from the Laraquete and Carampangue rivers is limited and nearshore wave energy is partially attenuated by the Arauco Peninsula and Isla Santa María (Fanucci et al., 1992; Gómez et al., 2018; Villagrán et al., 2023). This pattern aligns with the broader erosive trend documented along the south-central Chilean coast over recent decades, attributed to wave climate variability, relative sea-level rise under interseismic subsidence, and reduced fluvial sediment supply (Martínez et al., 2021). Critically, the pre-seismic shoreline time series (2000–2010) shows no discernible secular accretionary trend (Fig. 3b), confirming that autonomous sedimentary progradation was not operative at LHB under interseismic conditions.

Against this erosive background, the Extended Linear Trajectory Model (ELTM) isolates an instantaneous coseismic seaward displacement of 25 ± 4.9 m coinciding precisely with the 27 February 2010 Maule earthquake (Fig. 3b). The imposition of a positive Heaviside step on a system with no prior progradation trend constitutes robust evidence that tectonic

forcing, rather than sedimentary dynamics, drove the beach advance. This is consistent with the shoreface disequilibrium mechanism described by Anthony and Aagaard (2020), in which coseismic uplift generates an instantaneous relative sea-level fall, exposing previously submerged nearshore sands to subaerial reworking and initiating a transient onshore sediment flux.

Apparent divergences with DSAS-based seasonal studies (winter erosion, summer accretion) are methodological. The seasonal DSAS decomposition conflates oscillatory and trend components, and a high-tide proxy introduces systematic offsets comparable to the coseismic displacement; direct rate comparisons are therefore unreliable.

CoastSat (10–30 m pixel resolution, ±10 m positional uncertainty; Vos et al., 2019) resolves the event-scale coseismic step (25 ± 4.9 m), whereas the SVDL, digitised on sub-meter imagery (±0.5 m), captures the sustained multi-annual progradation (45–48 m) that integrates 15 years of beach–aeolian reconstruction. The SVDL is therefore the appropriate proxy for the dimensional comparison with strandplain inter-ridge spacing (48.9 m; Table S1).

The differential MSAVI2 response between zones, with seaward colonization in the NE zone versus vegetational stasis in the SW zone, further demonstrates that post-seismic coastal reconstruction is modulated by the pre-existing geomorphological configuration of each site rather than by differences in seismic forcing alone (Supplementary Material S.1, Figs. S1–S2; Fig. S3C).

5.2. Stratigraphic architecture of coseismic beach cycles: progradation-to-berm facies as the diagnostic tectonic imprint

The subsurface architecture revealed by GPR 1 and GPR 2 demonstrates that the 2010 coseismic event generated a diagnostic and spatially pervasive stratigraphic signature across LHB. In both profiles, the vertical succession of a Prograding Beach Facies (PBF) directly overlain by a Berm Beach Facies (BBF), locally incised by Runnel Channel Facies (RCF) structures, is identifiable at two distinct depth levels: one corresponding to the current post-seismic beach cycle and one corresponding to the pre-2010 earthquake beach cycle (Figs. 6, 7). The PBF, characterized by continuous seaward-dipping clinoforms (SWD reflectors), records the advancing beachface during a phase of shoreface progradation. The overlying BBF, defined by convex-up (CXU) and horizontal (H) high-amplitude reflectors at berm crest positions, records the stabilization of the upper beach once progradation decelerates and the berm consolidates. This PBF→BBF sequence therefore encodes the full morphodynamic arc of a single seismic beach cycle.

The abrupt landward decrease in radar signal amplitude further corroborates the episodic nature of this process. While recent deposits preserve high-amplitude reflections reflecting intact primary structures, the pre-earthquake facies transition sharply into attenuated signatures capped by low-amplitude Aeolian Facies (AF). This sharp contrast indicates discrete phases of rapid coastal abandonment, triggering subaerial stabilization, vegetation colonization, root bioturbation, and deposition of massive aeolian sand sheets (Ribolini et al., 2021; Rodríguez-Santalla et al., 2021). The diagnostic succession of each seismic beach cycle is therefore PBF→BBF, locally capped by AF where the aeolian sediment budget permits. The AF component is fully developed in the NE zone (GPR 1), where it forms a continuous drape landward of ~150 m, but remains a thin surface veneer insufficient to

constitute a distinct stratigraphic unit in the SW zone (GPR 2; Fig. 7d). This spatial contrast reflects cross-shore differences in aeolian sediment availability rather than a fundamental architectural difference between sectors.

The geometry of this succession is consistent between both profiles but differs markedly in spatial scale, reflecting the cross-shore asymmetry documented in the SVDL and topographic analyses. In GPR 1 (NE zone), the current beach cycle spans approximately 75 m and the pre-earthquake cycle approximately 50 m (Fig. 6d). In GPR 2 (SW zone), both cycles are spatially compressed, with the current cycle spanning ~20–25 m and the pre-earthquake cycle ~30–35 m (Fig. 7d). The presence of the complete PBF→BBF sequence at the GPR 2 transect, which records below-average post-seismic progradation relative to the multi-transect SVDL mean (21 m vs. 35.37 ± 11.25 m), confirms that the coseismic stratigraphic reorganization is a pervasive architectural feature of the system and not restricted to sectors of maximum accretion. LWD reflectors within the pre-earthquake BBF are exclusive to GPR 1, highlighting an additional asymmetry in berm architecture.

This PBF→BBF succession constitutes a modern analogue for the beach cycle architecture hypothesized to underlie each of the 52 beach ridges of the Laraquete–Carampangue strandplain (Araya-Cornejo et al., 2025). A direct dimensional test is provided by the inter-ridge spacing of the strandplain, measured from the same 1 m LiDAR DTM. Although 122 consecutive ridge pairs were initially analysed, application of a conservative 100 m threshold to exclude inter-patch digitization gaps retained 35 pairs representing true inter-ridge spacing (Table S1; Supplementary Material S.2). Minimum-distance measurements of these retained pairs yield a mean inter-ridge spacing of 48.9 m (95% CI BCa: 41.6–56.5 m; n = 35, median = 43.4 m, 95% CI BCa: 38.0–54.8 m; IQR = 32.6–63.9 m), dimensionally

consistent with the total post-seismic SVDL displacement documented at LHB (45.4 ± 4.0 m in the NE zone and 48.2 ± 10.4 m in the SW zone; Table 1).

Threshold sensitivity analysis (Supplementary Material S.2) confirms the robustness of this result: alternative thresholds of 75 m and 125 m yield mean spacings of 42.1 m and 51.3 m respectively, all within the uncertainty envelope of the post-seismic SVDL displacement. We therefore interpret this convergence as a dimensional compatibility between the modern analogue and the Holocene record, providing independent evidence that ridge–swale couplets are consistent with individual megathrust cycles, although a strict one-to-one correspondence requires absolute geochronological confirmation.

A note on dispersion is warranted: the coefficient of variation of Holocene inter-ridge spacing (CV ≈ 46%; 22.4/48.9 m) exceeds that of the modern post-seismic SVDL displacement (CV ≈ 11–32%; Table 1) by a factor of two to four. This higher dispersion likely reflects the cumulative effects of variable coseismic slip magnitude across successive Maule-type events, partial post-formation reworking of older ridges, and digitization uncertainty in the LiDAR-derived ridge polylines (Section S.2). Reporting both the mean (48.9 m) and the more robust median (43.4 m), both of which fall within the SVDL displacement range, accommodates this dispersion without compromising the dimensional comparison.

The reliability of swale floors as preserved inter-ridge markers is further supported by systematic crest-to-swale amplitude measurements conducted across contrasting progradational ridge plains (Shawler et al., 2025), confirming that swale geometry robustly records former inter-ridge depressions regardless of the coastal setting in which ridges formed.

The dimensional equivalence between post-seismic SVDL progradation (45–48 m) and mean inter-ridge spacing (48.9 m) requires that post-seismic progradation saturates well within the ~100-year seismic cycle. The reduced cross-shore spacing of the 2023–2025 SVDL positions in the NE zone relative to the 2017 line (Fig. 4a; Fig. 5a) is consistent with progressive deceleration of seaward advance, suggesting that ridge construction is approaching saturation within the 15-year observation window. This is independently supported by the abrupt landward signal attenuation in GPR 1, which records rapid coastal abandonment and subaerial stabilization (Fig. 6; Section 4.2).

5.3. A tectono-geomorphological model of post-seismic coastal construction: local synthesis and broader implications

The morphological, vegetational and stratigraphic evidence (Sections 4.1–4.3) converges into the three-stage conceptual model of Fig. 9. This model synthesizes the study and provides observational support for the coseismic strandplain-building mechanism of Araya-Cornejo et al. (2025), providing the first integrated morphodynamic and stratigraphic evidence that the Holocene process operates at human timescales and produces the predicted morpho-stratigraphic signature.

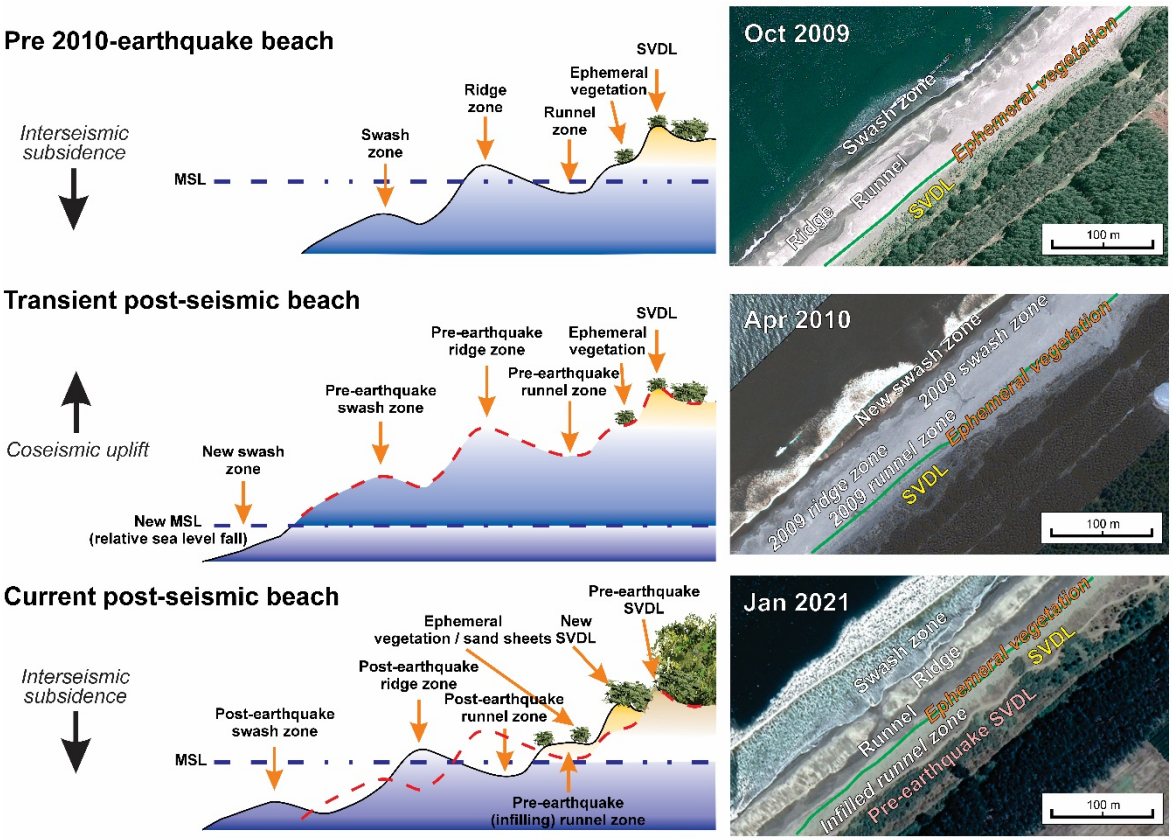

Fig. 9. Conceptual model of post-seismic beach evolution at Laraquete–Horcones Beach (LHB) following the 2010 Maule earthquake (Mw 8.8), illustrated across three stages. Left panels show idealized shore-normal cross-sections (schematic, not to scale); right panels show co-registered satellite imagery as empirical reference for each stage. (a) Pre-earthquake interseismic equilibrium (t_0 − 5 months; October 2009): the beach operates under slow interseismic subsidence with a well-developed ridge–runnel–SVDL sequence and no net secular progradation. (b) Coseismic disruption and transient emergence (t_0 + ~6 weeks; April 2010): coseismic uplift of ~1.5 m (Kelson et al., 2012) produces an instantaneous relative sea-level fall, stranding the pre-earthquake beach above the new MSL and exposing a new swash zone ~25 m seaward; two complete beach generations coexist at the surface. (c) Post-seismic reconstruction (t_0 + 15 years cumulative; example image from January 2021): a new ridge–runnel system has developed seaward of the abandoned pre-earthquake beach; the former runnel is progressively infilling and the backshore is being draped by aeolian sand sheets and nebkhas, initiating the sealing of the incipient beach ridge. MSL: mean sea level; SVDL: seaward dune vegetation line.

In Stage 1, the beach operates under interseismic subsidence in a state of dynamic equilibrium, with no net secular progradation and a well-developed ridge–runnel morphology that records the steady-state condition of a sediment-starved, tectonically subsiding coast (Section 4.1.1; Section 4.3.1). The pre-seismic ridge-and-runnel morphology documented at LHB (and independently at Isla Santa María; Aedo et al., 2023) serves as the direct geometric template from which the stranded beach ridge inherits its planform: the ridge crest becomes the incipient beach ridge and the runnel depression becomes the proto-swale (Carter, 1986; Shawler et al., 2025; Stanley, 1968). This ridge-and-runnel-to-crest-swale transformation is consistent with the progradational morphodynamics documented at dissipative barrier islands, where onshore bar migration generates analogous ridge-and-runnel systems subsequently preserved as crest–swale pairs (Shawler et al., 2025).

In Stage 2, the Mw 8.8 coseismic uplift produces an instantaneous base-level fall of ~1.5 m (Kelson et al., 2012), stranding the pre-earthquake beach above the new MSL and triggering abrupt shoreline progradation of ~25 m (Section 4.1.1).

In Stage 3, the post-seismic system reconstructs progressively: the SVDL advances 45–48 m (Section 4.1.2), the PBF→BBF succession records beachface progradation and berm consolidation (Section 4.2), and the aeolian facies drapes the backshore, sealing the incipient ridge crest with sand sheets and nebkhas (Section 4.2.1).

Net vertical displacement over each ~100-year seismic cycle is the prerequisite for permanent ridge preservation. The GPS stations closest to LHB (ARCO and HLPN; −9.8 mm yr^{-1}) yield a net tectonic gain of ~+0.5 m per cycle, sufficient to strand post-seismic morphologies above the active wave base. These two stations are spatially more

representative of the Gulf of Arauco coastline than PLVP; the higher subsidence rate at PLVP (−16.5 mm yr^{-1}) likely reflects intensified post-seismic viscoelastic relaxation due to its proximity to the zone of maximum coseismic slip (~12 m; Fig. 1b). This transient signal does not represent the long-term coastal deformation rate at the shoreline. Independently, the existence of 52 preserved ridge–swale couplets in the adjacent strandplain constitutes direct geomorphological evidence that net positive displacement has been sustained over successive Holocene cycles at this site. Together, these lines of evidence support the conclusion that the morphologies generated through Stages 1–3 escape complete marine reworking and become permanently incorporated into the strandplain architecture, building the Laraquete–Carampangue plain ridge by ridge over successive Holocene megathrust events.

In this context, coseismic uplift functions as a 'tectonic buffer': a recurrent mechanism that periodically offsets the combined effects of sediment deficit and interseismic subsidence, preventing net coastal retreat and sustaining long-term strandplain progradation under limited fluvial supply and accelerating sea-level rise. Although implicitly recognized in prior studies of convergent-margin strandplains (McSaveney et al., 2006; Pinegina et al., 2013; Tamura et al., 2007), we formalize it here as a unified conceptual framework for cross-system comparisons.

This mechanism is not unique to south-central Chile. The coexistence of stranded pre-seismic ridges and nascent post-seismic beaches following coseismic uplift has been documented after the 1964 Alaska earthquake (Stanley, 1968), the 2004 Sumatra–Andaman event (Monecke et al., 2015), the 2011 Tohoku-oki event (Tanaka et al., 2012), and the 2016 Kaikōura earthquake in New Zealand (MacDonald et al., 2023). What distinguishes the LHB–Laraquete–Carampangue system is the exceptional completeness of the record: 52

preserved ridge–swale couplets, a modern analog actively forming, and a subsurface stratigraphic architecture that links the two. This combination transforms the strandplain from a passive geomorphological feature into a potential paleoseismological archive, in which each ridge–swale pair encodes the magnitude, recurrence, and spatial extent of past megathrust ruptures (Kelsey et al., 2015; McSaveney et al., 2006; Pinegina et al., 2013).

6. Conclusions

Pre-seismic CoastSat-derived records confirm that Laraquete–Horcones Beach operated in a sediment-starved, interseismically subsiding state with moderate net erosion and no secular progradation prior to 2010. The Mw 8.8 Maule earthquake produced an instantaneous shoreline displacement of 25 ± 4.9 m, demonstrating that tectonic forcing, not sediment supply, drives progradation at this coast. Post-seismic SVDL mapping documents a sustained seaward advance of 45–48 m at rates two to three times the pre-seismic background, while UAV topography and GPR stratigraphy record a consolidated berm at 2.1–4.5 m a.s.l., nebkha microrelief of 0.1–0.3 m amplitude, and the diagnostic PBF→BBF stratigraphic succession, locally capped by an aeolian unit (AF) where the sediment budget permits.

The stratigraphic attribution of GPR facies to individual seismic cycles relies on geometric correlation with the SVDL record rather than on independent absolute geochronological control. Crucially, the abrupt landward attenuation of GPR signal amplitude provides independent geophysical evidence for episodic, coseismic coastal abandonment rather than continuous sedimentological progradation. Quantitative comparison between post-seismic SVDL displacement (45–48 m; Table 1) and mean strandplain inter-ridge spacing (48.9 m,

95% CI BCa: 41.6–56.5 m; Table S1, Fig. S4) is consistent with a single megathrust earthquake producing the morpho-stratigraphic equivalent of one Holocene beach ridge. The convergence of four complementary proxies provides the first multi-proxy observational evidence consistent with repeated coseismic uplift, rather than gradual sediment accumulation, driving Holocene strandplain construction along sediment-limited convergent margins, supporting this mechanism as a first-order control in sediment-starved convergent settings.

Coseismic uplift thus emerges as a recurring tectonic buffer (Section 5.3) that periodically resets the coastal system above a rising base level. Under accelerating sea-level rise, this mechanism acquires critical relevance: at sediment-limited convergent margins, episodic coseismic uplift represents a primary geomorphological mechanism sustaining long-term coastal progradation against chronic erosional forcing. Quantifying this tectonic buffer duration before interseismic subsidence reclaims the accreted surfaces is the primary knowledge gap for projecting long-term coastal resilience. Absolute dating of the GPR stratigraphic units and the 51 pre-2010 beach ridges by K-feldspar pIR-IRSL luminescence, which would transform the relative beach-ridge succession documented here into a quantitative record of megathrust recurrence intervals, and verification of the tectonic buffer mechanism at other convergent-margin strandplains constitute the primary directions for future research.

CRediT authorship contribution statement

Cristian Araya-Cornejo: Conceptualization, Methodology, Software, Validation, Formal analysis, Investigation, Writing – original draft, Visualization. **Diego Aedo:** Methodology, Investigation, Software, Validation, Writing – review & editing. **Carolina Martínez:**

Conceptualization, Writing – review & editing, Supervision, Funding acquisition. **Daniel Melnick:** Methodology, Writing – review & editing, Funding acquisition. **César Araya:** Software, Validation, Writing – review & editing. **Matías Carvajal:** Investigation, Writing – review & editing. **Arturo Belmonte:** Investigation, Writing – review & editing. **Marcos Moreno:** Resources, Investigation, Writing – review & editing. **Jorge Qüense:** Investigation, Writing – review & editing.

Declaration of competing interest

The authors declare that they have no known competing financial interests or personal relationships that could have appeared to influence the work reported in this paper.

Acknowledgements

This research was funded by the Agencia Nacional de Investigación y Desarrollo (ANID) through FONDECYT grant 1241922 and the Instituto Milenio en Socio-Ecología Costera (SECOS) grant ICN2019_015. D.A., D.M., C.A., M.C., and M.M. acknowledge the Millennium Nucleus CYCLO “The Seismic Cycle Along Subduction Zones” grant NC160025 and the Millennium Institute of Oceanography (IMO) grant ICN2025_030, both funded by the Millennium Science Initiative (ICM) of the Chilean Government, as well as the Chilean National Fund for Development of Science and Technology (FONDECYT) grant 1150321. C.A. and M.C. acknowledges ANID-FONDECYT grant 1231735. We thank Forestal Arauco for providing the LiDAR data under a confidentiality agreement with the CYCLO project.

Data availability

The CoastSat toolkit used for satellite-derived shoreline extraction is publicly available at https://github.com/kvos/CoastSat. Landsat and Sentinel-2 imagery are accessible through

Google Earth Engine (https://earthengine.google.com). The LiDAR DTM was acquired by Digimapas Chile and provided by Forestal Arauco under a research license and is not publicly available. All other datasets generated during this study — including multi-temporal SVDL vectors, CoastSat-derived shoreline time series, inter-ridge spacing measurements, shoreline change statistics, GPS vertical displacement series, bootstrap analysis script, and associated summary tables — are openly available in Zenodo at https://doi.org/10.5281/zenodo.20089893. The Google Earth Engine script used for MSAVI2 and EVI2 time-series analysis (Supplementary Material S.1) is available from the corresponding author upon reasonable request. UAV-derived topographic products are also available from the corresponding author upon reasonable request.

Declaration of generative AI and AI-assisted technologies in the writing process

During the preparation of this work the authors used Claude Sonnet 4.5 in order to improve the readability and language of the work. After using this tool/service, the authors reviewed and edited the content as needed and take full responsibility for the content of the published article.

References

Aedo, D., Cisternas, M., Melnick, D., Esparza, C., Winckler, P., Saldaña, B., 2023. Decadal coastal evolution spanning the 2010 Maule earthquake at Isla Santa Maria, Chile: Framing Darwin's accounts of uplift over a seismic cycle. Earth Surf. Process. Landf. 48, 2319–2333.

Albert, F., 1900. Las dunas del centro de Chile. Edición de la Pontificia Universidad Católica de Chile. Biblioteca Fundamentos de la Construcción de Chile, Santiago, Chile.

Anthony, E.J., Aagaard, T., 2020. The lower shoreface: Morphodynamics and sediment connectivity with the upper shoreface and beach. Earth. Sci. Rev. 210, 103334. https://doi.org/10.1016/j.earscirev.2020.103334

1045 Araya-Cornejo, C., Aedo, D., Martínez, C., Melnick, D., 2025. LiDAR and GPR Data Reveal
1046 the Holocene Evolution of a Strandplain in a Tectonically Active Coast. Remote Sens.
1047 (Basel). 17, 2798. https://doi.org/10.3390/RS17162798
1048 Bauer, B.O., Davidson-Arnott, R.G.D., 2003. A general framework for modeling sediment
1049 supply to coastal dunes including wind angle, beach geometry, and fetch effects.
1050 Geomorphology 49, 89–108. https://doi.org/10.1016/S0169-555X(02)00165-4
1051 Bertran, P., Andrieux, E., Bateman, M.D., Fuchs, M., Klinge, M., Marembert, F., 2020.
1052 Mapping and chronology of coversands and dunes from the Aquitaine basin, southwest
1053 France. Aeolian Res. 47, 100628. https://doi.org/10.1016/j.aeolia.2020.100628
1054 Bevis, M., Brown, A., 2014. Trajectory models and reference frames for crustal motion
1055 geodesy. J. Geod. 88, 283–311. https://doi.org/10.1007/S00190-013-0685-5
1056 Boak, E.H., Turner, I.L., 2005. Shoreline Definition and Detection: A Review. J. Coast. Res.
1057 21, 688–703. https://doi.org/10.2112/03-0071.1
1058 Carter, R.W.G., 1986. The morphodynamics of beach-ridge formation: Magilligan, Northern
1059 Ireland. Mar. Geol. 73, 191–214. https://doi.org/10.1016/0025-3227(86)90015-0
1060 Cohn, N., Ruggiero, P., de Vries, S., Kaminsky, G.M., 2018. New Insights on Coastal
1061 Foredune Growth: The Relative Contributions of Marine and Aeolian Processes.
1062 Geophys. Res. Lett. 45, 4965–4973. https://doi.org/10.1029/2018GL077836
1063 Cowell, P.J., Thom, B.G., 1995. Morphodynamics of coastal evolution. Coastal Evolution
1064 33–86. https://doi.org/10.1017/cbo9780511564420.004
1065 Crowell, M., Douglas, B.C., Leatherman, S.P., 1997. On Forecasting Future U.S. Shoreline
1066 Positions: A Test of Algorithms. J. Coast. Res. 13, 1245–1255.
1067 DaSilva, M., Silva, G.M. da, Hesp, P.A., Bruce, D., Keane, R., Moore, C., DaSilva, M., Silva,
1068 G.M. da, Hesp, P.A., Bruce, D., Keane, R., Moore, C., 2021. Assessing Shoreline
1069 Change using Historical Aerial and RapidEye Satellite Imagery (Cape Jaffa, South
1070 Australia). J. Coast. Res. 37, 468–483. https://doi.org/10.2112/JCOASTRES-D-20-
1071 00089.1
1072 Egbert, G.D., Erofeeva, S.Y., 2002. Efficient Inverse Modeling of Barotropic Ocean Tides. J.
1073 Atmos. Ocean. Technol. 19(2), 183–204.
1074 Fanucci, F., Amore, C., Pineda, V., 1992. Characteristics and dynamics of the coasts in the
1075 Arauco Gulf (Central Chile), in: Bollettino Di Oceanologia Teorica Ed Applicata. pp.
1076 265–271.
1077 Gómez, M., Villagrán, M., Martínez, C., Belmonte, A., 2018. Characterizing the longshore
1078 sediment transport pattern on beaches in the Gulf of Arauco, Chile, to assess
1079 morphological shoreline evolution. J. Coast. Res. 85, 656–660.
1080 Gorelick, N., Hancher, M., Dixon, M., Ilyushchenko, S., Thau, D., Moore, R., 2017. Google
1081 Earth Engine: Planetary-scale geospatial analysis for everyone. Remote Sens.
1082 Environ. 202, 18–27. https://doi.org/10.1016/j.rse.2017.06.031
1083 Hapke, C.J., Himmelstoss, E.A., Kratzmann, M., List, J.H., Thieler, R.E., 2010. National
1084 Assessment of Shoreline Change: Historical Shoreline Change Along the New England
1085 and Mid-Atlantic Coasts. U.S. Geological Survey, Reston, VA.
1086 Hesp, P., 2002. Foredunes and blowouts: initiation, geomorphology and dynamics.
1087 Geomorphology 48, 245–268. https://doi.org/10.1016/S0169-555X(02)00184-8
1088 Himmelstoss, E.A., Henderson, R.E., Kratzmann, M.G., Farris, A.S., 2018. Digital Shoreline
1089 Analysis System (DSAS) version 5.0 user guide. U.S. Geological Survey.
1090 Isla, M.F., Moyano-Paz, D., FitzGerald, D.M., Simontacchi, L., Veiga, G.D., 2023.
1091 Contrasting beach-ridge systems in different types of coastal settings. Earth Surf.
1092 Process. Landf. 48, 47–71. https://doi.org/10.1002/esp.5429
1093 Jarrin, P., Nocquet, J.M., Rolandone, F., Mora-Páez, H., Mothes, P., Cisneros, D., 2022.
1094 Current motion and deformation of the Nazca Plate: new constraints from GPS
1095 measurements. Geophys. J. Int. 232, 842–863. https://doi.org/10.1093/GJI/GGAC353

Kelsey, H.M., Witter, R.C., Engelhart, S.E., Briggs, R., Nelson, A., Haeussler, P., Corbett, D.R., 2015. Beach ridges as paleoseismic indicators of abrupt coastal subsidence during subduction zone earthquakes, and implications for Alaska-Aleutian subduction zone paleoseismology, southeast coast of the Kenai Peninsula, Alaska. Quat. Sci. Rev. 113, 147–158. https://doi.org/10.1016/j.quascirev.2015.01.006

Kelson, K., Witter, R.C., Tassara, A., Ryder, I., Ledezma, C., Montalva, G., Frost, D., Sitar, N., Moss, R., Johnson, L., 2012. Coseismic Tectonic Surface Deformation during the 2010 Maule, Chile, Mw 8.8 Earthquake. Earthquake Spectra 28. https://doi.org/10.1193/1.4000042

Kirkby, M.J., Kirkby, A. V., 1969. Erosion and deposition on a beach raised by the 1964 earthquake Montague Island, Alaska. Professional Paper, Professional Paper. https://doi.org/10.3133/pp543H

MacDonald, K.E., Hart, D.E., Pitman, S.J., 2023. Geomorphic responses of uplifted mixed sand and gravel beaches: combining short-term observations from Kaikōura, New Zealand with longer-term evidence. New Zealand Journal of Geology and Geophysics 66, 228–243. https://doi.org/10.1080/00288306.2021.1994425

Martínez, C., Rojas, D., Quezada, M., Quezada, J., Oliva, R., 2015. Post-earthquake coastal evolution and recovery of an embayed beach in central-southern Chile. Geomorphology 250, 321–333.

Martínez, C., Sepúlveda-Zúñiga, E., Villagrán, M., Rojas, O., Gómez, M., López, P., Rojas, C., 2021. Coastal evolution in a wetland affected by large tsunamigenic earthquakes in south-central chile: Criteria for integrated coastal management. Water (Switzerland) 13, 1467. https://doi.org/10.3390/w13111467

McSaveney, M.J., Graham, I.J., Begg, J.G., Beu, A.G., Hull, A.G., Kim, K., Zondervan, A., 2006. Late holocene uplift of beach ridges at turakirae head, south Wellington coast, New Zealand. New Zealand Journal of Geology and Geophysics 49, 337–358. https://doi.org/10.1080/00288306.2006.9515172

Medina Machín, A., Marcello, J., Hernández-Cordero, A.I., Martín Abasolo, J., Eugenio, F., 2019. Vegetation species mapping in a coastal-dune ecosystem using high resolution satellite imagery. GIsci. Remote Sens. 56, 210–232. https://doi.org/10.1080/15481603.2018.1502910

Melnick, D., Jara-Muñoz, J., Garrett, E., Plissart, G., Freisleben, R., Strecker, M.R., 2026. Separating tectonic and climate signals in Holocene sea-level records using marine terraces in central Chile. Sci. Rep. 16, 9083. https://doi.org/10.1038/s41598-026-43249-6

Mitchum, R.M., Vail, P.R., Sangree, J.B., 1977. Seismic Stratigraphy and Global Changes of Sea Level, Part 6: Stratigraphic Interpretation of Seismic Reflection Patterns in Depositional Sequences. Seismic Stratigraphy — Applications to Hydrocarbon Exploration. https://doi.org/10.1306/m26490c8

Monecke, K., Templeton, C.K., Finger, W., Houston, B., Luthi, S., McAdoo, B.G., Sudrajat, S.U., 2015. Beach ridge patterns in West Aceh, Indonesia, and their response to large earthquakes along the northern Sunda trench. Quat. Sci. Rev. 113, 159–170.

Neal, A., 2004. Ground-penetrating radar and its use in sedimentology: principles, problems and progress. Earth. Sci. Rev. 66, 261–330. https://doi.org/10.1016/j.earscirev.2004.01.004

Pettitt, A.N., 1979. A Non-Parametric Approach to the Change-Point Problem. Appl. Stat. 28, 126. https://doi.org/10.2307/2346729

Pinegina, T.K., Bourgeois, J., Kravchunovskaya, E.A., Lander, A. V., Arcos, M.E.M., Pedoja, K., MacInnes, B.T., 2013. A nexus of plate interaction: Vertical deformation of Holocene wave-built terraces on the Kamchatsky Peninsula (Kamchatka, Russia). GSA Bulletin 125, 1554–1568. https://doi.org/10.1130/B30793.1

Pirazzoli, P.A., 1995. Tectonic shorelines. Coastal Evolution 451–476. https://doi.org/10.1017/cbo9780511564420.014

Plafker, G., Savage, J.C., 1969. Mechanism of the May 21–22, 1960, Chilean Earthquakes as derived from residual vertical displacements. Eos, Transactions American Geophysical Union 50, 402–403. https://doi.org/10.1029/eo050i005p00402-03

Qi, J., Chehbouni, A., Huete, A.R., Kerr, Y.H., Sorooshian, S., 1994. A modified soil adjusted vegetation index. Remote Sens. Environ. 48, 119–126. https://doi.org/10.1016/0034-4257(94)90134-1

Ribolini, A., Bertoni, D., Bini, M., Sarti, G., 2021. Ground-penetrating radar prospections to image the inner structure of coastal dunes at sites characterized by erosion and accretion (Northern Tuscany, Italy. Applied Sciences 11, 11260.

Richmond, B., Szczuciński, W., Chagué-Goff, C., Goto, K., Sugawara, D., Witter, R., Tappin, D.R., Jaffe, B., Fujino, S., Nishimura, Y., Goff, J., 2012. Erosion, deposition and landscape change on the Sendai coastal plain, Japan, resulting from the March 11, 2011 Tohoku-oki tsunami. Sediment. Geol. 282, 27–39. https://doi.org/10.1016/j.sedgeo.2012.08.005

Rocha, T.B. da, Fernandez, G.B., Peixoto, M.N. de O., Rocha, T.B. da, Fernandez, G.B., Peixoto, M.N. de O., 2013. Applications of ground-penetrating radar to investigate the Quaternary evolution of the south part of the Paraiba do Sul river delta (Rio de Janeiro, Brazil). J. Coast. Res. 65, 570–575. https://doi.org/10.2112/si65-097.1

Rodríguez-Santalla, I., Gomez-Ortiz, D., Martín-Crespo, T., Sánchez, M.J., Montoya-Montes, I., Martín-Velázquez, S., Barrio, F., Serra, J., Ramírez-Cuesta, J.M., Gracia, F.J., 2021. Study and evolution of the dune field of la banya spit in ebro delta (Spain) using lidar data and gpr. Remote Sens. (Basel). 13, 1–17. https://doi.org/10.3390/rs13040802

San Martín, J., Calisto, I., Quezada, J., Stewart, D., Ely, L., Cifuentes-Lobos, R., Moreno, M., 2024. Characterization of historical megathrust earthquake ruptures in Central Chile using logic tree analysis. Natural Hazards 120, 5411–5427. https://doi.org/10.1007/S11069-024-06404-8/METRICS

Shawler, J.L., Hein, C.J., Georgiou, I.Y., Messina, F., Sakib, M.M., 2025. Local Versus Regional Controls on the Morphology and Texture of Preserved Beach and Foredune Ridges. J. Geophys. Res. Earth Surf. 130. https://doi.org/10.1029/2025JF008429

SHOA, 2025. Tablas de Marea del Territorio Chileno Antártico 2025-2026. Servicio Hidrográfico y Oceanográfico de la Armada de Chile.

Smyth, T.A.G., Wilson, R., Rooney, P., Yates, K.L., 2022. Extent, accuracy and repeatability of bare sand and vegetation cover in dunes mapped from aerial imagery is highly variable. Aeolian Res. 56, 100799. https://doi.org/10.1016/j.aeolia.2022.100799

Stanley, K.W., 1968. Effects of the Alaska earthquake of March 27, 1964, on shore processes and beach morphology. Professional Paper, Professional Paper. https://doi.org/10.3133/pp543J

Tamura, T., Nanayama, F., Saito, Y., Murakami, F., Nakashima, R., Watanabe, K., 2007. Intra-shoreface erosion in response to rapid sea-level fall: Depositional record of a tectonically uplifted strand plain, Pacific coast of Japan. Sedimentology 54, 1149–1162. https://doi.org/10.1111/j.1365-3091.2007.00876.x

Tanaka, H., Tinh, N.X., Umeda, M., Hirao, R., Pradjoko, E., Mano, A., Udo, K., 2012. Coastal and Estuarine Morphology Changes Induced by the 2011 Great East Japan Earthquake Tsunami. Coastal Engineering Journal 54. https://doi.org/10.1142/S0578563412500106

Tsunetaka, H., Murakami, W., Daimaru, H., 2024. Shoreline advance due to the 2024 Noto Peninsula earthquake. Scientific Reports 2024 14:1 14, 28026-. https://doi.org/10.1038/s41598-024-79044-4

Villagrán, M., Gómez, M., Martínez, C., 2023. Coastal Erosion and a Characterization of the Morphological Dynamics of Arauco Gulf Beaches under Dominant Wave Conditions. Water (Switzerland) 15. https://doi.org/10.3390/w15010023

Vos, K., Splinter, K.D., Harley, M.D., Simmons, J.A., Turner, I.L., 2019. CoastSat: A Google Earth Engine-enabled Python toolkit to extract shorelines from publicly available satellite imagery. Environmental Modelling & Software 122, 104528. https://doi.org/10.1016/j.envsoft.2019.104528

Wesson, R.L., Melnick, D., Cisternas, M., Moreno, M., Ely, L.L., 2015. Vertical deformation through a complete seismic cycle at Isla Santa María, Chile. Nat. Geosci. 8, 547–551.

Supplementary Material S.1. — MSAVI2 Vegetation Dynamics Analysis

S.1.1. Rationale

The seaward advance of the dune vegetation line (SVDL), mapped from high-resolution optical imagery at 11 epochs (Section 3.3, main text), provides a multi-decadal record of the geomorphological response at LHB, but does not capture the progressive, pixel-level spectral signal of pioneer vegetation establishment across the full beach–aeolian transect. To independently corroborate and spatially characterize the post-seismic vegetation colonization documented by the SVDL analysis, a time series of the Modified Soil-Adjusted Vegetation Index 2 (MSAVI2; Qi et al., 1994) was extracted along the two GPR transect coordinates for the full study period 2002–2025, using medium-resolution multispectral satellite imagery. This analysis is entirely independent of the SVDL mapping in terms of data source, spatial scale, and detection principle, and is designed to confirm that the SVDL advance reflects genuine ecological succession rather than a digitization artefact or a regional climate signal.

S.1.2. Satellite Imagery and Index Selection

Vegetation dynamics along both study transects were characterized using MSAVI2 (Qi et al., 1994), computed from annual median composites of Landsat Collection 2 Surface Reflectance imagery (2002–2014) and Sentinel-2 MSI (S2SRHARMONIZED; 2015–2025) processed in Google Earth Engine (Gorelick et al., 2017). The sensor transition year (2015) was defined by the availability of Sentinel-2 imagery over the study area. For the Landsat archive, scenes from Landsat 5 TM, Landsat 7 ETM+, Landsat 8 OLI, and Landsat 9 OLI-2 were included as available per year, processed using the Collection 2 Level-2 surface reflectance algorithm and scaled to physical reflectance values (scale factor: 0.0000275, offset: −0.2). Cloud and cloud-shadow masking was applied to all Landsat images using the QA_PIXEL band (bits 3 and 4), and to Sentinel-2 images using the QA60 band (bits 10 and 11), retaining only scenes with less than 30% cloud cover. Annual composites were generated as pixel-wise medians of all cloud-masked scenes within each calendar year.

MSAVI2 was selected over conventional ratio-based indices such as NDVI because its adaptive soil-correction factor minimizes the confounding effect of bare soil and sandy substrate on the vegetation signal, a critical advantage in coastal aeolian environments where sparse or pioneer vegetation coexists with extensive unvegetated sandy surfaces (Qi et al., 1994; Medina Machín et al., 2019). MSAVI2 is computed as:

$$\mathrm{MSAVI2} = \frac{2 \cdot \mathrm{NIR} + 1 - \sqrt{(2 \cdot \mathrm{NIR} + 1)^2 - 8(\mathrm{NIR} - \mathrm{Red})}}{2}$$

where NIR and Red are the near-infrared and red surface reflectance values, respectively. This formulation makes MSAVI2 particularly suited for detecting early-stage and low-density vegetation colonization under conditions of high soil brightness, where NDVI systematically underestimates cover. The robustness of MSAVI2 in coastal aeolian ecosystems has been demonstrated in vegetation mapping studies where it outperformed 22 other spectral indices under conditions of low and heterogeneous cover on sandy substrates (Medina Machín et al., 2019).

To independently characterize and compare the pre-earthquake vegetation baseline conditions between both sites, the Two-Band Enhanced Vegetation Index (EVI2; Jiang et al., 2008) was computed as a complementary diagnostic index. EVI2 was selected because it exhibits greater sensitivity at very low canopy cover fractions and maintains a more linear response to leaf area index under sparse vegetation conditions, making it better suited for quantifying subtle differences in near-zero cover. As EVI2 does not require a blue band, it is directly applicable to the full Landsat 5/7/8/9 and Sentinel-2 time series without additional atmospheric corrections. The EVI2 analysis was restricted to the pre-earthquake period (2002–2009) and applied simultaneously to both transects.

S.1.3. Spatial Sampling and Profile Extraction

Both indices were sampled along the exact coordinates of the GPR survey transects (Profile 1: NE transect, 190 m total length; Profile 2: SW transect, 100 m total length). Sampling was performed at 10 m spatial resolution using the GEE .sample function applied to each annual median composite, with point geometries returned for subsequent distance calculation. For each sampled point, the along-transect distance from the seaward origin was computed using geodesic distance calculations referenced to the first transect vertex, and binned at 10 m intervals. Annual mean MSAVI2 and EVI2 values were computed per distance bin and assembled into year × distance pivot matrices. Years with no available imagery (data gaps) were filled by cubic spline interpolation over the gap years, bounded by the nearest valid observations, with linear interpolation applied where fewer than four valid years were available. All analysis was restricted to the transect segment co-located with the GPR survey profile (0–190 m for Profile 1; 0–100 m for Profile 2).

S.1.4. Statistical Analysis and Cross-Sensor Validation

Inter-sensor consistency at the 2015 Landsat-to-Sentinel-2 transition was assessed using a Mann-Whitney U test comparing the distributions of annual mean MSAVI2 values immediately before (2012–2014) and after (2015–2017) the sensor transition. This test was applied to MSAVI2 and to three additional indices (NDVI, MNDWI, NDWI2) to identify which index best preserved temporal continuity across the sensor change. MSAVI2 was the only index that showed no statistically significant discontinuity attributable to the sensor transition (Mann-Whitney U, $p = 1.0$), confirming its suitability as the primary index for the full 2002–2025 time series.

Temporal trend analysis was conducted using the non-parametric Mann-Kendall test (Mann, 1945; Kendall, 1975) applied to the annual mean MSAVI2 time series. To avoid confounding the ecological trend with the sensor transition, the Mann-Kendall test was first applied exclusively to the Landsat-only period (2002–2014), providing a trend estimate entirely independent of Sentinel-2 data. Sen's slope estimator (Sen, 1968) was used to quantify the magnitude of the monotonic trend in units of MSAVI2 per year. A structural change-point in the time series was identified using the non-parametric Pettitt test (Pettitt, 1979), which detects the most probable year of abrupt shift in the central tendency of the series without requiring distributional assumptions. The Pettitt test was applied to the full 2002–2025 time series. All statistical tests were performed at a significance level of $\alpha = 0.05$.

Period-averaged spatial profiles were computed by averaging the annual MSAVI2 pivot matrices within three ecologically defined periods: pre-earthquake (2002–2009), transition

(2010–2014), and post-colonization (2015–2025), with ±1 standard deviation envelopes reflecting inter-annual variability within each period.

S.1.5. Results

S.1.5.1. Profile 1 (NE zone, 190 m)

The spatio-temporal heatmap of Profile 1 reveals a marked seaward advance of vegetation cover of several tens of metres initiated between 2010 and 2014, spatially concentrated in the sector closest to the shoreline (0–90 m from the seaward origin; Fig. S1A). Prior to the 2010 Maule earthquake, MSAVI2 values in this zone were consistently low (mean = 0.05), consistent with an active beach and foreshore subject to regular marine inundation that precluded vegetation establishment. The pre-earthquake stability of near-zero MSAVI2 values across the entire eight-year baseline (2002–2009) demonstrates that the seaward sector was persistently hostile to vegetation prior to the earthquake; the abrupt onset of the colonization signal within two to four years of the 2010 event, under otherwise unchanged regional climate conditions, is consistent with a tectonic rather than a climatic trigger.

A statistically significant structural change-point was detected in 2014 (Pettitt test, $p < 0.0001$), one year before the sensor transition, confirming that the observed trend reflects genuine ecological succession and cannot be attributed to the change in sensor platform (Fig. S1B). The Mann-Kendall trend test applied exclusively to the Landsat-only period (2002–2014) corroborates this interpretation, revealing a strong monotonic increase in MSAVI2 ($\tau = 0.821$, $p < 0.0001$, slope = 0.0044 yr^{-1}) that predates any Sentinel-2 contribution to the time series. Spatial profiles by period (Fig. S1C) demonstrate that the seaward expansion of vegetation progressed from the stable interior sand sheet (90–190 m; Fig. S3C) toward the newly exposed coastal fringe, a pattern diagnostic of progressive substrate stabilization following marine retreat induced by coseismic uplift rather than interannual climatic variability.

S.1.5.2. Profile 2 (SW zone, 100 m)

Profile 2 did not yield a statistically significant vegetation trend across the study period (Mann-Kendall, Landsat-only: $\tau = 0.077$, $p = 0.76$; post-change-point: $\tau = 0.018$, $p = 1.0$; Fig. S2B). Although a formal Pettitt change-point was detected at 2015 ($p < 0.0001$), this breakpoint coincides exactly with the Landsat-to-Sentinel-2 sensor transition and, in the absence of any pre- or post-transition trend, is interpreted as a subtle sensor-related radiometric discontinuity rather than an ecological signal. The three period-averaged spatial profiles are largely overlapping across the full transect length, confirming the absence of a post-seismic colonization gradient at this site (Fig. S2C).

The EVI2 pre-earthquake baseline analysis (Fig. S3C) provides the quantitative confirmation: while both profiles show near-zero EVI2 values in their proximal seaward sectors (0–30 m), confirming that both sites were equally hostile to vegetation prior to the earthquake, Profile 1 maintained a well-developed interior vegetation reservoir between 100–190 m (mean EVI2 = 0.20–0.25) that is structurally absent in Profile 2, whose total sandsheet extent (100 m) precludes the existence of an equivalent landward source. This null result is interpreted as ecologically consistent: although coseismic uplift occurred at both sites, uplift alone was insufficient to drive seaward vegetation colonization at Profile 2 without a proximate vegetation reservoir to supply propagules and without the substrate extent necessary for aeolian buffering. Profile 2 was included to ensure methodological

transparency and to demonstrate that the vegetation changes at Profile 1 are not a regional or sensor-driven artefact; the absence of a parallel trend at an adjacent site subjected to the same satellite processing pipeline and the same seismic event reinforces the site-specific, ecologically mediated nature of the colonization response documented in the NE zone.

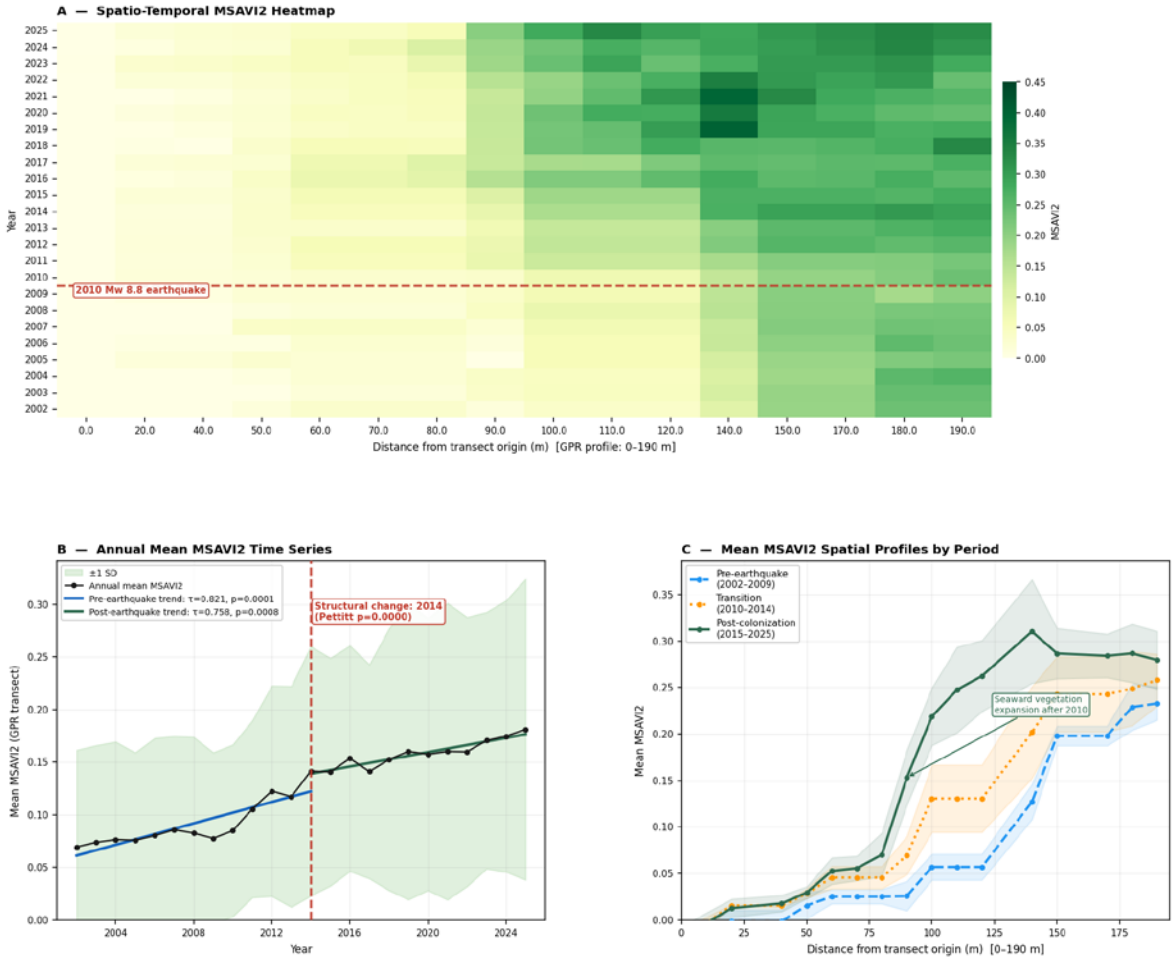

Fig. S1. Spatio-temporal analysis of MSAVI2 along GPR 1 Profile (NE zone; 0–190 m from the seaward origin), co-located with the ground-penetrating radar survey profile. (A) Annual median MSAVI2 heatmap (2002–2025) derived from Landsat Collection 2 Surface Reflectance (2002–2014) and Sentinel-2 MSI S2SRHARMONIZED (2015–2025) composites processed in Google Earth Engine. The dashed red horizontal line marks the 2010 Mw 8.8 Maule earthquake. Post-seismic greening concentrated in the seaward sector (0–90 m) reflects pioneer vegetation colonization of newly exposed substrate. (B) Annual mean MSAVI2 time series averaged across the full GPR transect (±1 SD shading). Blue and dark green lines show OLS trend fits for the pre-earthquake (2002–2014; Mann-Kendall $\tau = 0.821$, $p < 0.0001$) and post-change-point (2014–2025; $\tau = 0.758$, $p < 0.0008$) periods, respectively. The dashed red vertical line marks the Pettitt-detected structural change-point (2014; $p < 0.0001$), which precedes the Landsat-to-Sentinel-2 sensor transition by one year, confirming that the observed trend reflects genuine ecological succession rather than a sensor artefact. (C) Mean MSAVI2 spatial profiles by period (±1 SD shading). The progressive upward displacement of the post-colonization profile (2015–2025, dark green) relative to the pre-earthquake baseline (2002–2009, blue dashed) in the

seaward sector (0–90 m) is diagnostic of substrate stabilization and pioneer vegetation establishment following coseismic marine retreat.

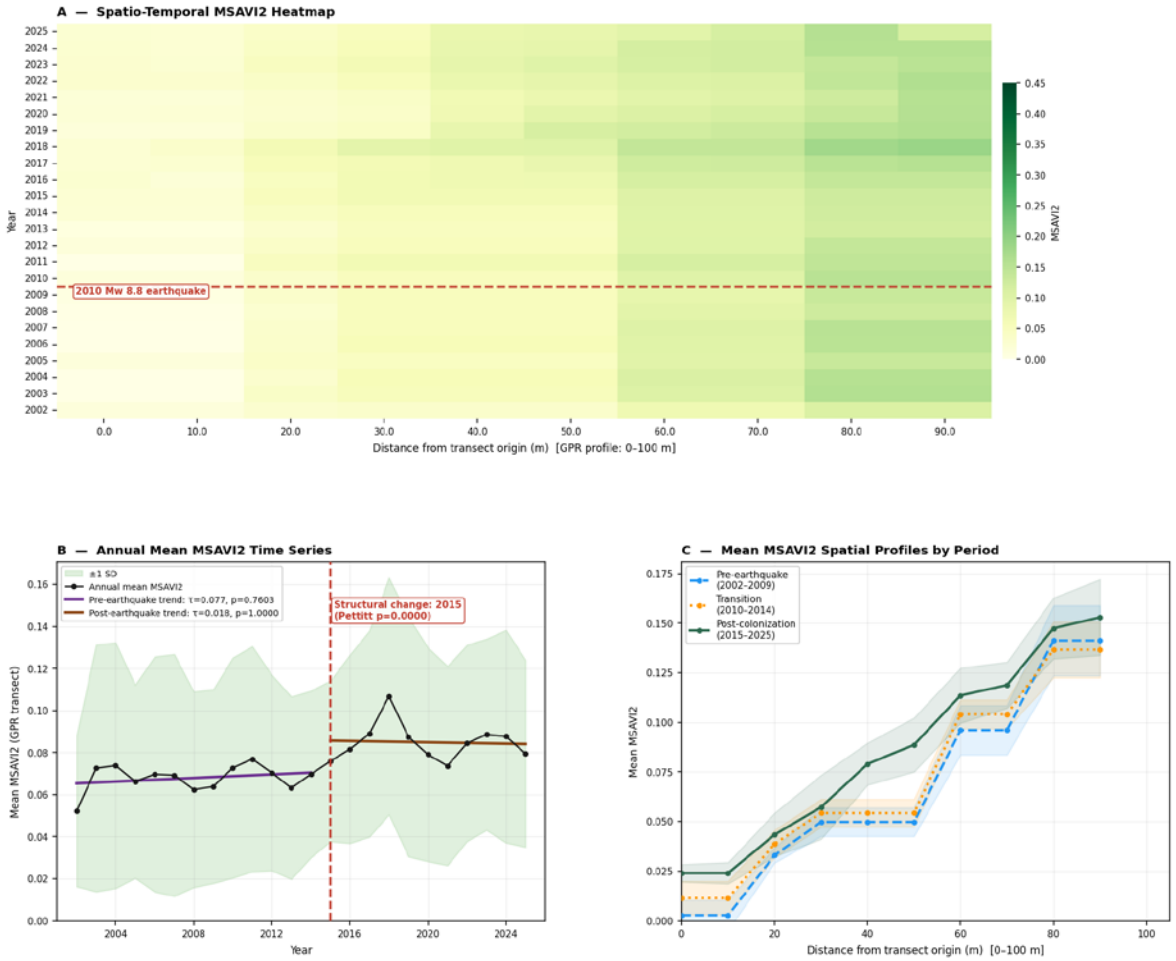

Fig. S2. Spatio-temporal analysis of MSAVI2 along GPR 2 Profile (SW zone; 0–100 m from the seaward origin), co-located with the GPR survey profile. (A) Annual median MSAVI2 heatmap (2002–2025). The dashed red horizontal line marks the 2010 Mw 8.8 Maule earthquake. No progressive seaward greening is detectable following the earthquake. (B) Annual mean MSAVI2 time series (±1 SD shading). Both the pre-earthquake Mann-Kendall trend (2002–2014; $\tau = 0.077$, $p = 0.76$) and the post-change-point trend ($\tau = 0.018$, $p = 1.0$) are non-significant. The Pettitt-detected structural change-point at 2015 ($p < 0.0001$) coincides exactly with the Landsat-to-Sentinel-2 sensor transition and is interpreted as a minor radiometric discontinuity rather than an ecological signal. (C) Mean MSAVI2 spatial profiles by period (±1 SD shading). The three period profiles are largely overlapping across the full transect length, confirming the absence of a post-seismic colonization gradient, ecologically consistent with the intrinsically narrower aeolian sandsheet and the absence of a landward vegetation reservoir at this site (see Fig. S3C).

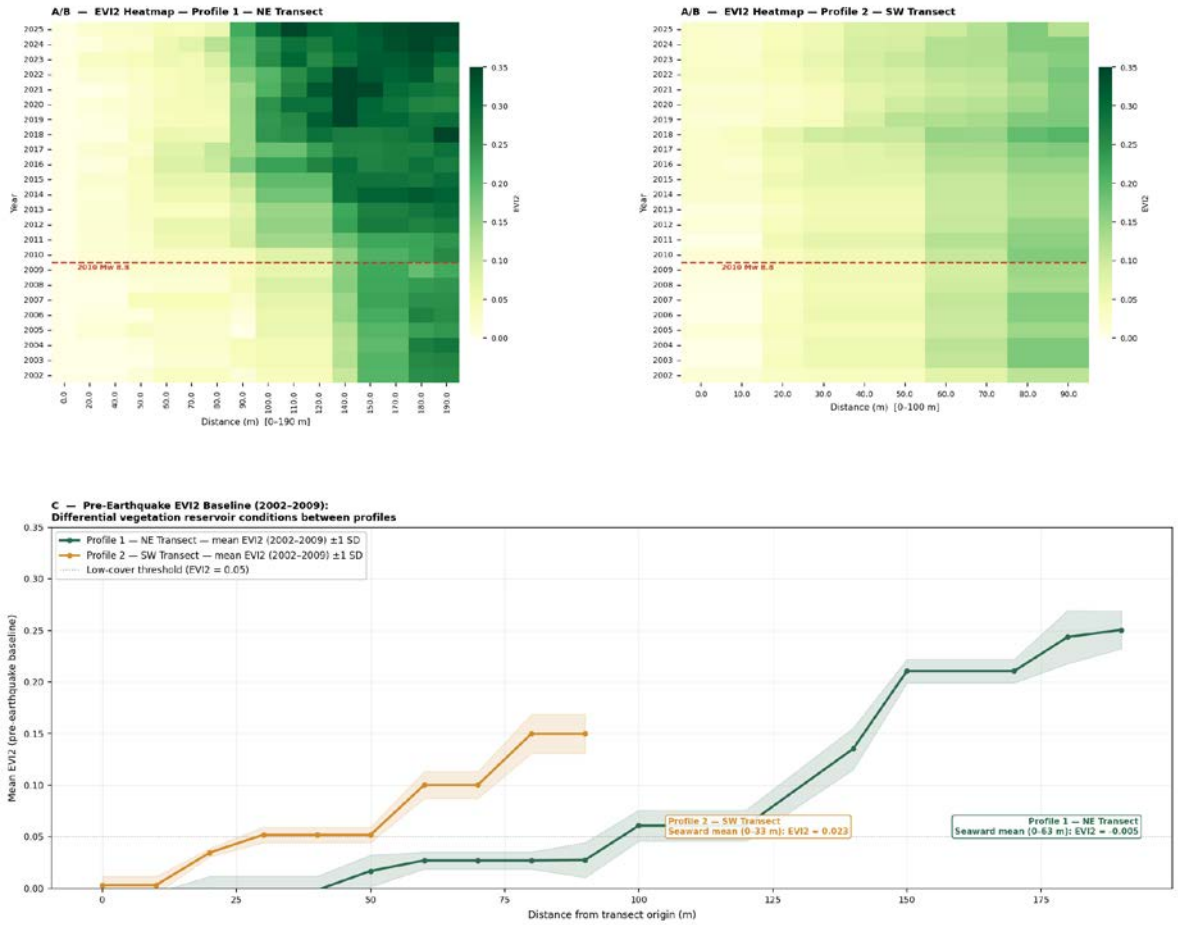

Fig. S3. Two-Band Enhanced Vegetation Index (EVI2; Jiang et al., 2008) analysis used as an independent index to characterize and compare pre-earthquake vegetation baseline conditions between Profile 1 (NE transect, 190 m) and Profile 2 (SW transect, 100 m). EVI2 was computed from the same Landsat Collection 2 and Sentinel-2 MSI imagery used for MSAVI2 analysis. (A–B) Annual median EVI2 heatmaps (2002–2025) for Profile 1 and Profile 2, respectively. The dashed red horizontal line marks the 2010 earthquake. Profile 1 shows a clear post-seismic increase in EVI2 in the seaward sector after 2010, consistent with MSAVI2 results (Fig. S1A). Profile 2 shows no comparable progressive greening pattern. (C) Pre-earthquake EVI2 spatial profiles (2002–2009 mean ±1 SD) for both transects on a common distance axis. While both profiles show near-zero EVI2 values in the proximal seaward sector (0–30 m), confirming active beach conditions at both sites prior to the earthquake, Profile 1 maintains a well-developed interior vegetation reservoir (100–190 m; mean EVI2 = 0.20–0.25) that is structurally absent in Profile 2. This differential pre-seismic vegetation reservoir, rather than overall cover magnitude, is interpreted as the primary factor controlling the contrasting post-earthquake colonization responses documented in Figs. S1–S2.

S.1.6. References

Bezerra, F.G.S., Moura, M.S.B., Melão Brandão Vasconcelos, M.F., Siqueira, J.O., Gomes, D.J.C. (2020). Analysis of areas undergoing desertification, using EVI2 multi-temporal data based on MODIS imagery as indicator. *Egyptian Journal of Remote Sensing and Space Sciences*, 23(1), 87–94.

Earth Resources Observation and Science (EROS) Center. (2020). *Landsat Collection 2 Level-2 datasets*. U.S. Geological Survey.

Gorelick, N., Hancher, M., Dixon, M., Ilyushchenko, S., Thau, D., Moore, R. (2017). Google Earth Engine: Planetary-scale geospatial analysis for everyone. *Remote Sensing of Environment*, 202, 18–27.

Jiang, Z., Huete, A.R., Didan, K., Miura, T. (2008). Development of a two-band enhanced vegetation index without a blue band. *Remote Sensing of Environment*, 112(10), 3833–3845.

Kendall, M.G. (1975). *Rank correlation methods* (4th ed.). Griffin.

Mann, H.B. (1945). Nonparametric tests against trend. *Econometrica*, 13(3), 245–259.

Medina Machín, A., Marcello, J., Hernández-Cordero, A.I., Martín-Abasolo, J., Eugenio, F. (2019). Vegetation species mapping in a coastal-dune ecosystem using high resolution satellite imagery. *GIScience & Remote Sensing*, 56(2), 210–232.

Pettitt, A.N. (1979). A non-parametric approach to the change-point problem. *Applied Statistics*, 28(2), 126–135.

Qi, J., Chehbouni, A., Huete, A.R., Kerr, Y.H., Sorooshian, S. (1994). A modified soil adjusted vegetation index. *Remote Sensing of Environment*, 48(2), 119–126.

Sen, P.K. (1968). Estimates of the regression coefficient based on Kendall's tau. *Journal of the American Statistical Association*, 63(324), 1379–1389.

Supplementary Material S.2. — Inter-Ridge Spacing Analysis of the Laraquete–Carampangue Strandplain

S.2.1. Rationale

The one-ridge-per-earthquake hypothesis predicts that the cross-shore width of a single post-seismic beach cycle should be dimensionally equivalent to the spacing between adjacent beach ridges preserved in the Holocene strandplain. To test this prediction quantitatively, the inter-ridge spacing of the Laraquete–Carampangue strandplain was measured directly from the same 1 m resolution LiDAR DTM (Digimapas Chile, 2004–2007) used to derive the geomorphological map (Fig. 2, main text) and the pre-seismic topographic profiles (Fig. 8, main text), allowing an independent dimensional comparison with the post-seismic SVDL displacement documented in Section 4.1.2.

S.2.2. Data and Processing

Beach ridge geometries were represented as 123 polylines digitized from the LiDAR DTM hillshade and slope derivatives in QGIS 3.x, originally produced for the geomorphological map of Araya-Cornejo et al. (2025). All analyses were performed in Python 3.x using geopandas 1.0.1 and shapely, projected in UTM Zone 18S (EPSG:32718) to ensure metric distance calculations.

Ridge ordering. Ridges were ordered from seaward to landward using principal component analysis (PCA) of centroid coordinates. The shore-normal direction was defined as the eigenvector of minimum variance of the centroid cloud, and each centroid was projected onto this axis to obtain a scalar cross-shore position. This approach is fully data-driven and requires no a priori definition of the shore-normal azimuth.

Distance calculation. Inter-ridge spacing was computed as the minimum geometric distance between each consecutive pair of ridge polylines (n = 122 pairs). Minimum geometric distance was preferred over centroid-to-centroid distance because it measures the actual gap between ridge bodies rather than the distance between their longitudinal midpoints, which can be sensitive to along-shore ridge curvature and digitization length.
Exclusion threshold. Of 122 consecutive ridge pairs, 87 (71.3%) yielded distances exceeding 100 m and were excluded from statistical analysis. Inspection of the raw distribution (Fig. S4, right panel) reveals a clear bimodal structure: a compact cluster of values between 0 and ~100 m, and a dispersed population extending up to 7,091 m. The latter population reflects inter-patch digitization gaps between laterally discontinuous ridge segments across different longitudinal sectors of the strandplain, that is, the geometric distance between the end of one digitized ridge segment and the beginning of the next ridge segment in a different sector, rather than true inter-ridge cross-shore distances. A conservative threshold of 100 m was selected to fully separate these two populations while retaining all plausible inter-ridge distances given the known coastal progradation scale (~45–48 m; Table 1, main text). The 35 retained pairs represent sectors of continuous, laterally traceable ridge sequences. Because continuous sectors tend to correspond to well-preserved portions of the strandplain, the retained sample may carry a modest conservative bias toward regular, well-expressed ridge spacings; this does not affect the validity of the dimensional comparison with the SVDL record. Thus, the final statistical analysis was performed on the 35 retained pairs that represent true inter-ridge cross-shore distances.

Threshold sensitivity analysis. To assess the sensitivity of the mean inter-ridge spacing to the choice of threshold, the analysis was repeated at thresholds of 75 m, 100 m, and 125 m, yielding retained samples of 22, 35, and 42 pairs and mean spacings of 42.1 m, 48.9 m, and 51.3 m, respectively. Across this range, the mean spacing remains within ±3.0 m of the 48.9 m value reported in the main text, and in all cases falls within the uncertainty envelope of the post-seismic SVDL displacement (45–48 m; Table 1, main text). This confirms that the dimensional equivalence between the modern seismic beach cycle and the Holocene inter-ridge spacing is robust to the specific threshold adopted. The 100 m threshold was retained as the primary value because it corresponds to the visual inflection point of the bimodal distribution (Fig. S4, right panel), maximally separates the two populations, and is conservative relative to the known progradation scale.

S.2.3. Results

Statistical descriptors for the 35 retained ridge pairs are summarized in Table S1.

Table S1. Descriptive statistics of inter-ridge spacing for the Laraquete–Carampangue strandplain (retained pairs, threshold ≤ 100 m).

Statistic	**Value (m)**
n (valid pairs)	35

Mean	48.9
95% CI bootstrap BCa (mean)	41.6–56.5
Median	43.4
95% CI bootstrap BCa (median)	38.0–54.8
Standard deviation	22.7
Minimum	0.0
Maximum	97.8
25th percentile (Q1)	32.6
75th percentile (Q3)	63.9
IQR	32.6–63.9

The mean (48.9 m, 95% CI BCa: 41.6–56.5 m; n = 35) and median (43.4 m, 95% CI BCa: 38.0–54.8 m) inter-ridge spacing are statistically indistinguishable from the total post-seismic SVDL displacement documented at LHB: 45.4 ± 4.0 m in the NE zone and 48.2 ± 10.4 m in the SW zone (Table 1, main text). The IQR (32.6–63.9 m) encompasses the full range of post-seismic NSM values recorded across all transects in both zones, including the minimum (21 m, GPR 2 transect) and the maximum (~60 m in the SW zone high-progradation sectors). The near-zero minimum (0.0 m) reflects two ridge polylines that share a boundary vertex in the digitized dataset and should be interpreted as a single composite ridge rather than two distinct features with zero separation (Fig. S4).

Bootstrap BCa confidence intervals (10,000 replicates, seed = 42) were computed for both estimators. The post-seismic SVDL displacement range (45–48 m; Table 1, main text) falls within both the mean CI (41.6–56.5 m) and the median CI (38.0–54.8 m), confirming dimensional compatibility between the modern seismic beach cycle and the Holocene inter-ridge spacing regardless of the central tendency estimator used.

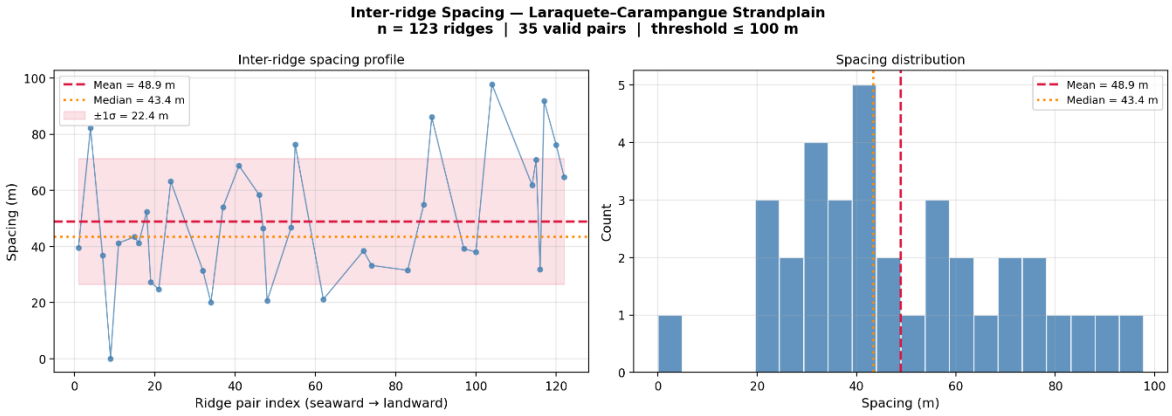

Fig. S4. Inter-ridge spacing distribution of the Laraquete–Carampangue strandplain. Minimum geometric distance between 35 consecutive beach ridge polyline pairs retained after applying a 100 m exclusion threshold, derived from the 1 m LiDAR

DTM (Digimapas Chile, 2004–2007; EPSG:32718). *Left panel:* spacing profile ordered from seaward (index 1) to landward ridge pairs. Red dashed line: mean (48.9 m); orange dotted line: median (43.4 m); shaded band: ±1σ (22.4 m). *Right panel:* frequency distribution of retained spacings. Of 122 consecutive ridge pairs, 87 (71.3%) exceeded the 100 m threshold and were excluded; these values reflect inter-patch digitization gaps between laterally discontinuous ridge segments rather than true inter-ridge distances (see Section S2.2. for exclusion criteria). The grey shaded band in the left panel indicates the range of total post-seismic SVDL progradation documented at LHB (45–48 m; Table 1, main text), showing dimensional equivalence between the modern seismic beach cycle and the mean inter-ridge spacing of the Holocene strandplain.

Supplementary Material S.3. — Regional GPS Vertical Displacement Analysis

S.3.1. Rationale

The tectono-geomorphological model presented in this study (Fig. 9, main text) predicts that the post-seismic beach progradation occurs against a background of ongoing interseismic subsidence. To independently quantify the rate and character of this long-term vertical motion, vertical displacement time series from three continuous GPS stations (ARCO, PLVP and HLPN) located within ~50 km of the study area were analysed. These stations are operated by the Nevada Geodetic Laboratory (UNR) and provide high-precision daily solutions that capture both the early post-seismic relaxation phase and the subsequent steady-state interseismic subsidence. This analysis provides quantitative support for the interseismic subsidence component of Stage 1 (dynamic equilibrium) and for the effectiveness of coseismic uplift as a temporary tectonic buffer against relative sea-level rise.

S.3.2. Data and Processing

Daily position time series (North, East, Up components) in the IGS14 reference frame were downloaded from the Nevada Geodetic Laboratory (NGL) Station Pages. Only the vertical (Up) component was used. Data span the period 2010–2025 and were processed with the GIPSY-OASIS software using precise point positioning with ambiguity resolution. A combined log-linear model was fitted to the vertical displacement time series of each station using non-linear least-squares optimization. The functional form is:

$$u(t) = a\ln\,(t + b) + c + d \cdot \frac{t}{1 + e^{-t/\tau}}$$

where the first term captures the early post-seismic logarithmic relaxation and the second term represents the long-term interseismic linear trend with a smooth transition controlled by the parameter τ. This approach avoids an arbitrary break-point and provides a continuous description of both the transient and steady-state phases. The long-term interseismic subsidence rate was calculated from the last 8 years of the time series to represent the steady-state condition. All displacements were referenced to the first available epoch of each station.

S.3.3. Results

The vertical displacement time series and combined fits are presented in Fig. S5. All three stations show rapid initial logarithmic subsidence followed by a steady linear trend. The

long-term interseismic subsidence rates are –9.8 mm yr⁻¹ (ARCO), –16.5 mm yr⁻¹ (PLVP) and –9.8 mm yr⁻¹ (HLPN). These rates are notably faster than those reported for many other convergent margins (e.g., ~2–4 mm yr⁻¹ in the northeastern USA) and confirm that the south-central Chilean coast continues to subside at a significant rate more than 15 years after the 2010 event.

Table S2. Long-term interseismic subsidence rates derived from the combined model (last 8 years of the time series).

Station	Latitude (°S)	Longitude (°W)	Rate (mm yr⁻¹)	±1σ (mm yr⁻¹)
ARCO	37.206	73.226	–9.8	0.1
PLVP	37.149	73.585	–16.5	0.0
HLPN	36.748	73.190	–9.8	0.0

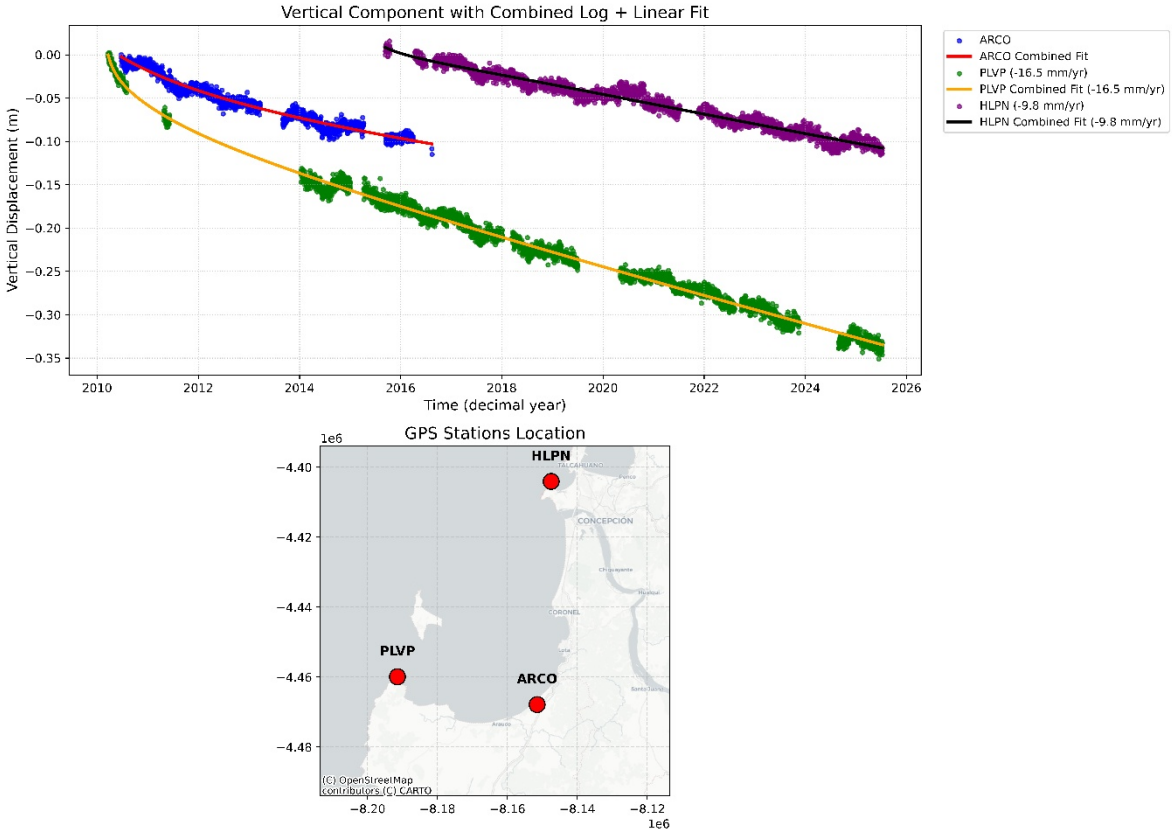

Fig. S5. Combined GPS analysis of vertical displacement at stations ARCO, PLVP and HLPN (Nevada Geodetic Laboratory). (A) Time series of vertical displacement (m) referenced to the first available epoch of each station. Coloured points: daily solutions. Solid lines: best-fit combined log-linear model. The long-term interseismic subsidence rates (mm yr⁻¹) are indicated in the legend for each station. (B) Location map of the three GPS stations relative to the study area (LHB, red outline). The inset shows the regional tectonic setting. Note that the long-term subsidence rates of –9.8 to –16.5 mm yr⁻¹ provide quantitative confirmation of the ongoing interseismic subsidence component in the three-stage model (Fig. 9, main text) and underscore the role of coseismic uplift as a temporary tectonic buffer against relative sea-level rise.

These GPS-derived rates represent regional interseismic deformation patterns; site-specific subsidence at LHB may differ slightly due to local structural heterogeneity, though the available geodetic network provides the best available constraint for this coastal segment.